Alteration of Wetting Properties of Orthopaedic Titanium Alloy (Ti-6Al-7Nb) using Laser Shock Peening

Shen, X., Shukla, P., Swanson, P., An, Z., Prabhakaran, S., Waugh, D., Nie, X., Mee, C., Nakhodchi, S. & Lawrence, J.

Original citation & hyperlink:
Shen, X, Shukla, P, Swanson, P, An, Z, Prabhakaran, S, Waugh, D, Nie, X, Mee, C, Nakhodchi, S & Lawrence, J 2019, 'Alteration of Wetting Properties of Orthopaedic Titanium Alloy (Ti-6Al-7Nb) using Laser Shock Peening', Journal of Alloys and Compounds, vol. 801, pp. 327-342.
https://dx.doi.org/10.1016/j.jallcom.2019.06.104

DOI 10.1016/j.jallcom.2019.06.104
ISSN 0925-8388
ESSN 1873-4669

Publisher: Elsevier

Altering the Wetting Properties of Orthopaedic Titanium Alloy (Ti-6Al-7Nb) using Laser Shock Peening

Xiaojun Shen[a*], Pratik Shukla[a], Philip Swanson[a], Zhibin An[b], S. Prabhakaran[c], , David Waugh[a], Xiangfan Nie[d] Christopher Mee[e], Soheil Nakhodchi[f], and Jonathan Lawrence[a]

[a] Coventry University, School of Mechanical, Aerospace and Automotive Engineering, Faculty of Engineering, Environment and Computing, Priory Street, Coventry, CV1 5FB, UK.

[b] Science and Technology on Plasma Dynamics Laboratory, Air Force Engineering University, Xi`an, P.R. China

[c]Centre for Crystal Growth, Department of Physics, School of Advanced Sciences, Vellore Institute of Technology, Vellore, 632014, Tamilnadu, India

[d] School of Mechanical and Power Engineering, East China University of Science and Technology, Shanghai 200237, China

[e]Coventry University, Department of Bimolecular and Sport Sciences, Priory Street, Coventry, CV1 5FB, UK.

[f] K.N. Toosi University of Technology, Mechanical Engineering Faculty, Tehran, Iran.

Corresponding Author: *Email s673864902@126.com

ABSTRACT

This work focuses on exploiting the effects of laser shock peening (LSP) to control the wetting characteristics of bio-material surfaces integrated with surface characteristics such as surface energy, macro and nano-topography. In particular, the effects of laser energy and beam footprint overlap of LSP were explored on Ti-6Al-7Nb alloy, quantified by using the measurement of dynamic contact angle, followed by determination of the surface-free energy and the work of adhesion. Surface modification by LSP was conducted at laser energy of 3J, 5J, 7J, & overlap of 33%, 50%, 67% at 3mm laser spot diameter. An incremental hole drilling method was employed for near to surface residual stress measurement. The results showed that compressive residual stress of between -42MPa to -516 MPa were formed on the sub-surface of LSPned Ti-6Al-7Nb. The results showed that surface roughness, surface-free energy and work of adhesion were proportional to laser energy, contact angle, however, was found to be inversely proportional to laser energy at consistent overlap. Additionally, surface-free energy and work of adhesion are proportional to overlap, but surface roughness and contact angle have a negative correlation with overlap. The correlation between laser energy and contact angle can be explained by Wenzel's theory while the relationship between overlap and contact angle is described by Cassie-Baxter model. This investigation on effects of LSP on the wetting characteristics not only addresses the required parameters for cell response on LSP modified titanium alloys, but also identifies that a metallic material strengthening process such as laser shock peening can also modify the wettability of a solid metallic surface as well as benefit the mechanical properties of metallic implants.
Keywords: Ti-6Al-7Nb; Laser Shock Peening; Wettability; Surface Roughness; Contact angle; Surface-free energy; work of adhesion;

1. Introduction

Ti-6Al-7Nb titanium alloy has been widely employed in clinical application due to its excellent biocompatible and outstanding mechanical properties [1-3]. However, due to variety reasons such as aseptic loosen [4], fracture [5], wear and corrosion [6], the implants could fail inside human body after the first clinical surgery, resulting in another replacement surgery which is highly risks and money costly. To avoid or delay the need for a secondary surgery, it is necessary to prolong the service life of implants which not only requires improved mechanical properties, but also the biocompatibility of titanium alloy. After implantation, titanium and its alloys initially react with the host tissue that the reaction determines the healing speed or long-term performance of the implants. This performance depends on the physicochemical parameters of implant surfaces including surface free energy, wettability, and surface roughness. These surface properties, especially wetting characteristics, have a great influence on the cell/protein adhesion, growth, proliferations and differentiations after being inserted into the human body in the early stage. Therefore, it is crucial to acquire a suitable surface wettability for the success of a clinical implantation. And these wetting characteristics are mainly determined by the material itself. But, by means of surface modification methods, the surface wettability could be changed within some extend range, even from hydrophilic to super-hydrophobic [7-9]. For example, Balaur et al [10-11] showed that self-organized nanotubular oxide layers lead to surperhydrophilics surfaces by changing nanotube diameters. In terms of medical implants biomaterial, Gentelmen [12] and Groth [13] reported that 60º-70º contact angle of material surfaces benefits cell the integration of cell/implants and 65º contact angle is thought to be an ideal levels of cell attachment and spreading.

Silva *et al* [14] found that roughening surfaces could introduce physico-chemical changes thereby affecting the surface free energy and wettability. A comparative high surface roughness may lead to the increase of local surface stress concentrations. Therefore, acquiring biocompatible surface topography is important as a modification method with respect to attaining optimum bio-metallic interfacial properties.

Laser shock peening (LSP), as an effective surface improvement method for metal, has been continuously been applied in aerospace industry for over 60 years since it was firstly invented [15-16]in 1950s. It has been successfully applied in improving the metallic characteristics such as wear-resistance, corrosion resistance and fatigue life [17-20]. In recent years, researchers have started to seek a new application for LSP namely the medical industry. Mannava *et al.* [21] applied LSP on the spinal implant rod to increase fatigue strength in order to decrease the back pain of end user. Caralapatti *et al*. [22] and Guo *et al*. [23] found that the corrosion resistance of biodegradable magnesium and magnesium-calcium alloys could be enhanced by LSP. Additionally, the fatigue performance of Mg-Ca alloy subject to LSP was also improved, as observed by Sealy *et al* [24]. Zhang et al [25] also demonstrated the tensile and

fatigue strength of AZ31B magnesium alloy was significantly increased via LSP. Furthermore, in the previous work [26], the mechanical properties such as wear resistance of Ti-6Al-7Nb alloy used for hip replacement were improved by repeated laser shock peening.

More recently, most research on medical metals (magnesium and titanium) subject to LSP are focusing on the improvement of mechanical properties. However, in terms of the effects of LSP parameters (laser energy and overlap) on wettability of titanium alloy, the research is still unknown and unreported. As the metallic manufactured implants would integrate with cells/proteins in *vivo,* the surface wettability of laser shock peened (LSPned) metals must be also evaluated. On account of this, the effect of two LSP parameters (laser energy and overlap) on the wettability characteristics of Ti-6Al-7Nb titanium alloy are investigated for the first-time. In addition, results correlate and integrate with studies of topography, microstructure and determination of the surface-free energy and work of adhesion of orthopaedic titanium samples subject to LSP. This work will develop optimum LSP processing parameters for acquiring a suitable surface wetting characteristics which will be seen as a fundamental factor of further cell adhesions.

2. Material and methods

2.1 Material characterization methods

2.1.1 Ti-6Al-7Nb alloy and sample preparation for SEM

The experimental material was a titanium alloy (Ti-6Al-7Nb) made with standard specification ASTM 1295 rod bar, that was made by Aircraftmaterials co., Ltd, Stokenchurch, UK. The chemical composition of the material was Nb 6.5-7.5(wt%), Al 5.5 - 6.6 (wt%), Ta <0.5 (wt%), Fe <0.25 (wt%), O <0.2 (wt%), C <0.08 (wt%), N <0.05 (wt%), H <0.009(wt%), and Ti Bal (wt%). The as-received samples with diameter of 25.4mm (1 inch) bar (see Figure 1(a)) were cut into small disks with thickness of 3mm. They were then polished from 120 grid to 1200 grid using SiC papers. In terms of etching method, after polishing, 3 samples as the untreated group were taken directly into distilled water with ultrasonic cleaning for 5 minutes. Thereafter, they were immersed in 100 ml beaker in 20ml concentrated Kroll`s reagent for 20s in the fume hood. The LSPned samples, it is the same way to etch LSPned samples. Microstructural analysis was performed with a Scanning Electron Microscope ((SEM) Sigma 500Vp. Zeiss SMT AG; Germany) at the accelerated voltage of 5KV with SE2 signal.

2.1.2 Residual stress measurement by Incremental hole drilling and 3D profiling evaluation

The cross-section residual stress measurements were carried out by using an incremental hole drilling method with a system designed by Stress measurement, UK. The strain relaxation was measured by a standard three-gauge rosette (90º×2, 45 º×1) manufactured by VPG Ltd, US. The diameter dimension of the drilled hole was around 2mm, and the depth is about 1mm. Strain relaxation was recorded with

14 increments (initially 4 increments of 32µm, then 4 increments of 64µm, finally 8 increments of 128µm). All increments data, Young`s modulus of 105GPa and Poisson's ration of 0.36 were interpreted and calculated by Stresscraft RS INT software for the residual stress measurements.

A 3-D Profiling station motion system (Contour GT-K, Bruker, Germany.) was employed to measure surface topography of Ti-6Al-7Nb alloy. The mapping was carried with x5 lens at x2 magnification. Scanning strategy starts from the left corner on the LSPned surfaces then taking zigzags routine for acquiring finally a rectangle map with the size of 10 × 10 mm^2.

2.2 Laser shock peening parameters

The LSP experiments were conducted by a Q-Switched Nd:YAG laser, using a wavelength of 1064 nm and 20 ns pulse width. As laser energy and spot overlapping are two main parameters in LSP, they are selected as variables in this work. The pulse energy was tested at 3J, 5J&7J and at each level energy, spot overlapping was 33%, 50%, 67%. The experimental and theoretical LSPned samples images are shown in Figure 1. The laser spot size was 3 mm. Thus, the power densities were 2.13 Gw/cm^2, 3.54 Gw/cm^2, 4.95Gw/cm^2. The radiance density (laser beam brightness) parameter as determined using our previous method [27-29] equated to 0.46, 0.77 and 1.09 (W. Cm^2.Sr.µm) respectively as detailed in Table.1. The water layer was used as the confinement layer, while absorbtive layer was polyvinyl black tape. Figure 1 (a) presents a schematic diagram of LSP, (b) as-received Ti-6Al-7Nb rod bar and (c), a the schematic of LSP strategy process

Table 1 LSP parameters employed for the surface treatment of Ti-6Al-7Nb.

Parameters	Value
Pulse energy (J)	3, 5, 7,
Laser wavelength (nm)	1064
Spot diameter (mm)	3
Number of laser impacts	1
Overlapping rate (%)	33%,50%,67%
Pulse duration (ns)	20
Radiance Density ($W.mm^2.Sr.\mu m$)	0.46 @ 3J 0.77 @ 5J 1.09 @ 7J

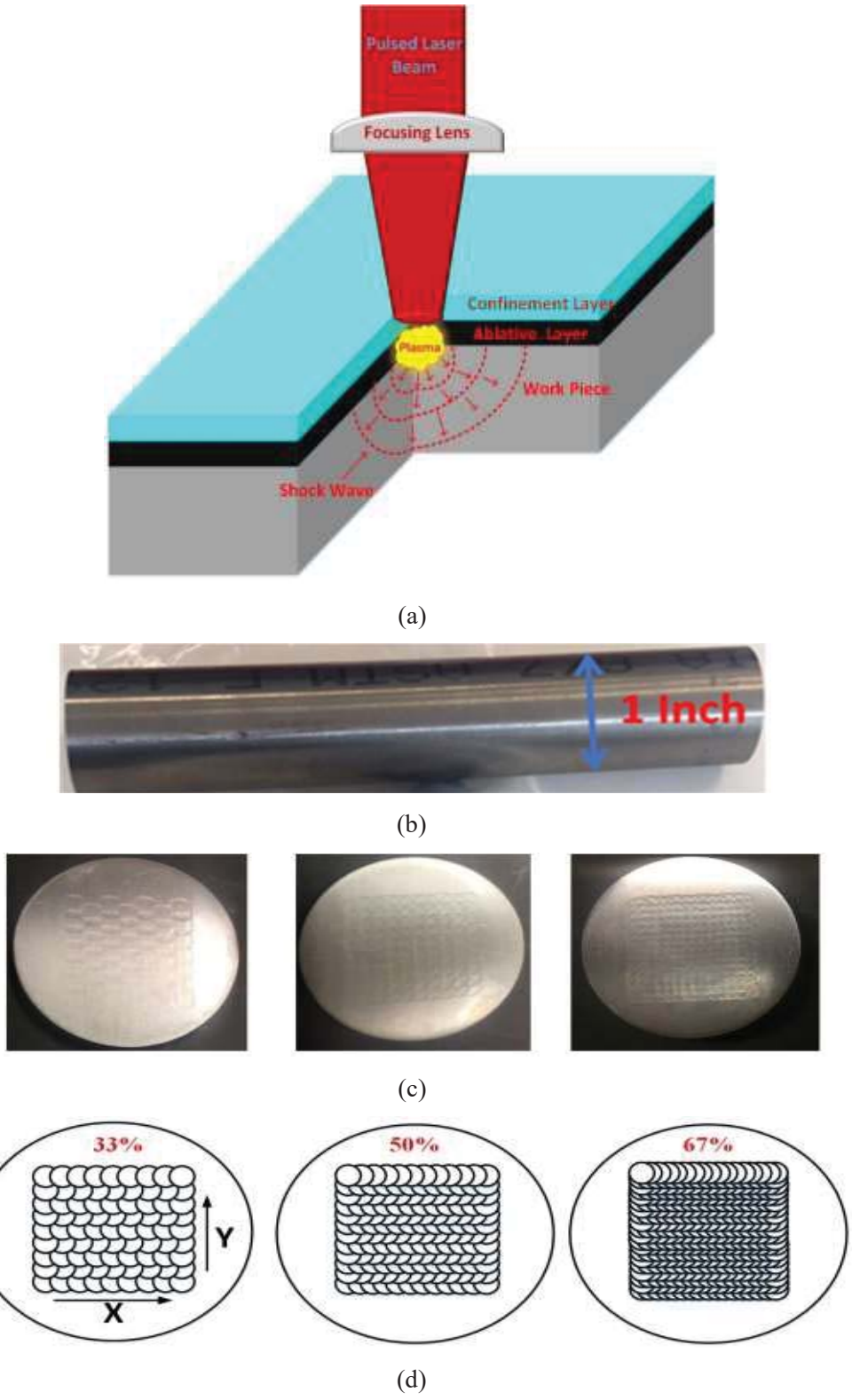

Figure 1. A 3-D schematic diagram of Laser Shock Peening process in (a); the as-received titanium rod bar in (b); the laser shock peened surfaces in (c) and the schematics of the laser shock peening strategy in (d).

2.3 Analysis of Wettability

The wetting circumstance is normally characterized by Contact Angle (CA) which describes the surface tension at the interface amongst the three-phase (liquid/gas/solid) system, as shown in Figure 2. This interaction can be described by using the Young`s equation

$$\gamma_{SG} = \gamma_{SL} + \gamma_{LG} \cos\theta \quad \text{..... (1)}$$

Where $\cos\theta$ is a single-valued equilibrium contact angle; $\gamma_{SG}, \gamma_{SL}, \gamma_{LG}$ are the solid/gas, solid/liquid, liquid/ gas interfacial tensions.

However, the Young`s equation can only be applied under the assumption that the surface is homogenous, physically and chemically inert to the liquid. Whereas, in real surfaces, due to the surface roughness, there is more than one equilibrium contact angle on the surface. Therefore, in terms of real surfaces which have asperities greater than 0.5 μm, the dynamic contact angle including advancing and receding contact angle are employed as the equilibrium contact angle [30].

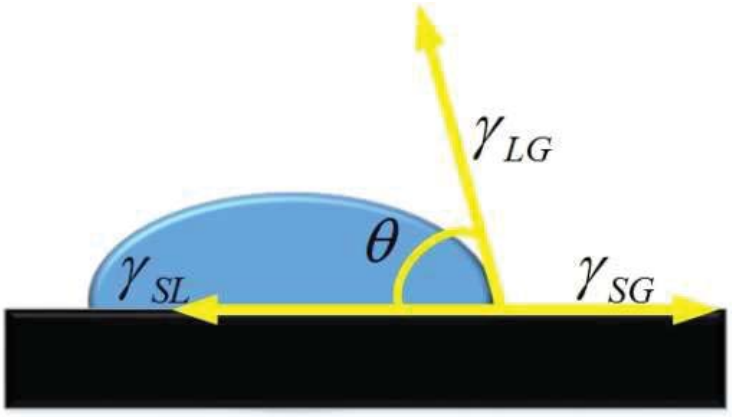

Figure 2 Surface tension equilibrium balance as described by Young`s equation.

2.3.1 Hysteresis measurement

Dynamic contact angles are produced in the course of wetting or de-wetting, which represented as advancing angle and receding angle separately which results in the contact angle Hysteresis (2) [31].

$$H = \theta_{Ad} - \theta_{Re} \quad \text{..... (2)}$$

Where θ_{Ad} is advancing contact angle and θ_{Re} is receding contact angle. The contact angle hysteresis H is also defined as arithmetic difference which describes the wetting ability of the surface.

It should be noted that the advancing angle has been commonly used for calculating the surface interfacial tensions as the surface roughness has less influence on the advancing contact angle, compared to the receding contact angle [30].

In order to acquire the advancing contact angle, the sessile drop goniometric method was used *via* a instrument OSCA100developed by Data Physics co., Ltd, Germany. The measurement was taken automatically, by filming in the course of wetting (advance angle) from de-wetting (receding angle) at the room temperature (22±2℃). The needle-in method was employed for dynamic contact angle data. At first, a liquid droplet of 0.5µl was dosed onto the surface by syringe pump. Then, 10µl of liquid with the inserting velocity of 0.5µl/s was continuously pumped onto the surface, expanding the volume of the original drop for a period of 20s. After that, the drop would remain stable as the syringe stops pumping in liquid for 10s. By the end, all liquid would revert back into the syringe with the same velocity. During whole procedure, the images were recorded (for subsequent) analysis by a Software (SCA 20) for dynamic contact angle quantification. Typical advancing and receding contact angle data is shown in the Figure 3. The advancing and receding angle are separately the mean value of the contact angle during the wetting and de-wetting course. The schematic images of advancing angle and receding angle are shown in Figure 4.

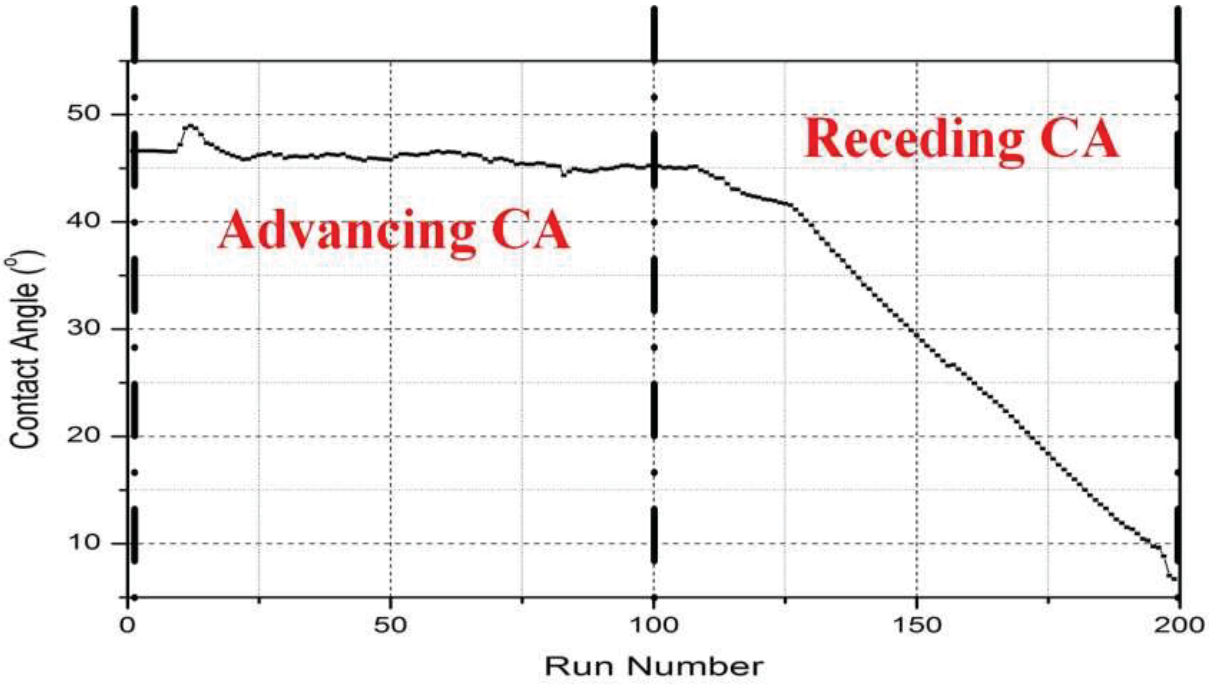

Figure 3: The typical advancing angle and receding angle collected from the contact angle plot diagram.

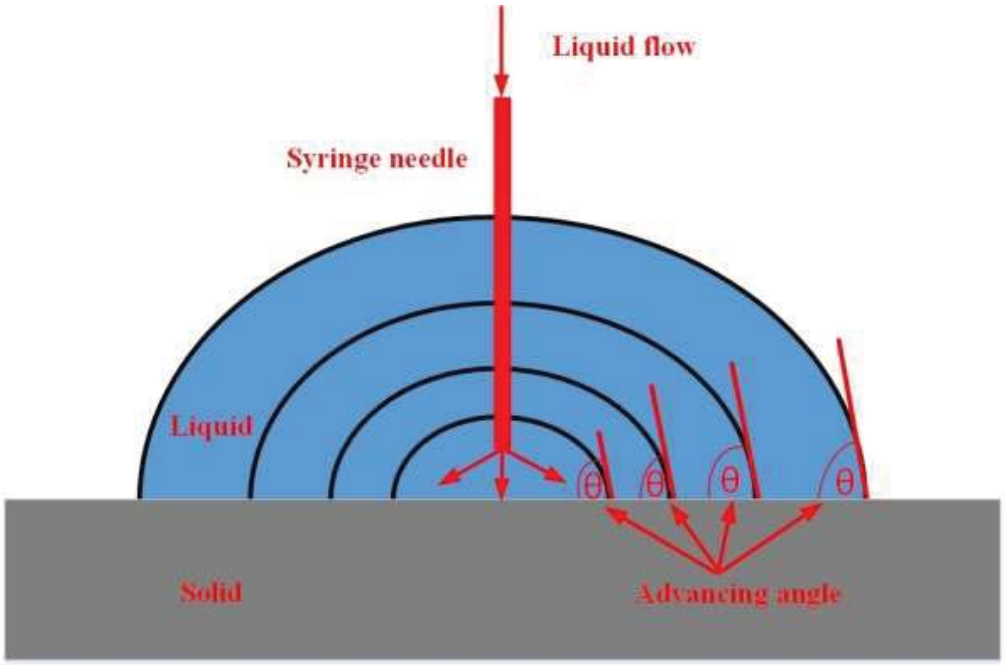

(a)

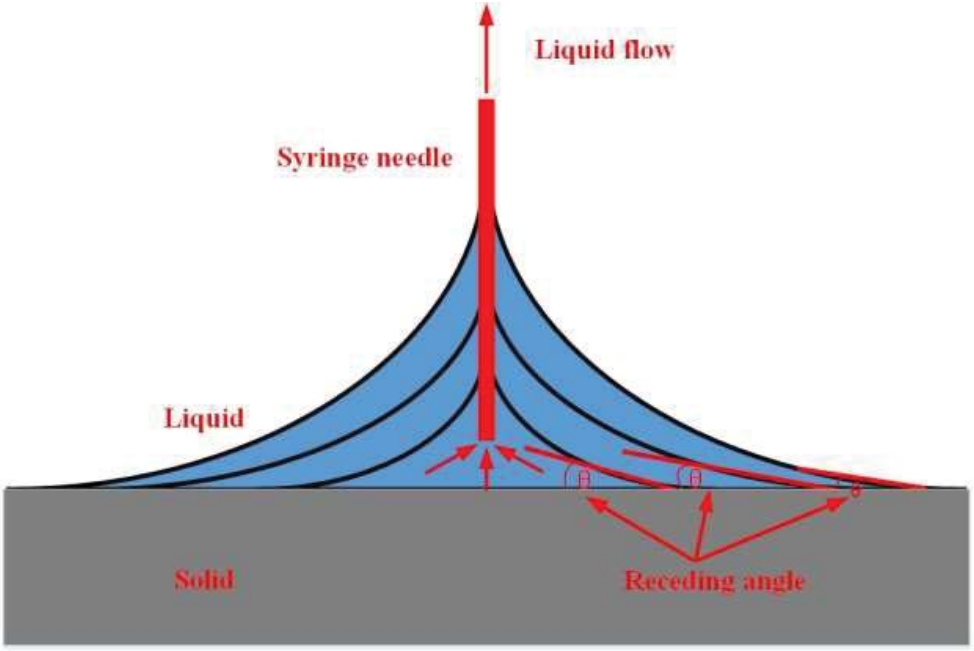

(b)

Figure 4: Schematic images showing the advance angle in (a), and the receding angle in (b)

2.3.4 Surface free energy

By dropping different test liquids onto the solid surface, the surface-free energy (SFE) of a solid can be calculated using several theoretical models such as Fowkes method [32], Owen-Wendt method [33] and Van Oss-Chaudhury-Good method [34]. In this work, Owens-Wendt-Rabel-Kaeble (OWRK) model was selected to quantitate the surface-free energy [35]. This equation is as follows:

$$\gamma_{SL} = \gamma_S + \gamma_L - 2\sqrt{\gamma_S^d \gamma_L^d} - 2\sqrt{\gamma_S^p \gamma_L^p} \quad \text{(3)}$$

Where γ_{SL} is the interfacial tension of solid/liquid tension, γ_S is the solid-free energy, γ_S^d is the dispersive component and γ_S^p is the polar component of the solid surface-free energy. γ_L^d is dispersive aspect of test liquid surface tension and γ_L^p is polar part of test liquid surface tension. Combined with Young`s equation, equation (4) is acquired below:

$$\underbrace{\frac{\gamma_L(1+\cos\theta)}{2\sqrt{\gamma_L^d}}}_{y} = \underbrace{\sqrt{\gamma_S^p}}_{m} * \underbrace{\sqrt{\frac{\gamma_L^p}{\gamma_L^d}}}_{x} + \underbrace{\sqrt{\gamma_S^d}}_{c} \quad \text{(4)}$$

The total surface-free energy γ^T is consist of the sum of polar components γ^p and the γ^d dispersive components, as shown in the equation (5)；

$$\gamma^T = \gamma^p + \gamma^d \quad \text{(5)}$$

Therefore, to quantitate the surface-free energy of a solid surface including polar part and dispersive part, at least two kinds of test liquid are needed. In this work, distilled water and ethylene glycol were employed for calculating the total surface-free energy. The values of surface-free energy, and its components for distilled water and ethylene glycol are shown in Table 2.

Table 2 The surface free energy (γ^T), polar part (γ^p) and dispersive part (γ^d) of distilled water and ethylene glycol.

	Total surface energy mN/m	Dispersive part mN/m	Polar part mN/m
Distilled water	72.8	21.8	51
Ethylene glycol	48	29	19

2.3.3 Work of adhesion

The work of adhesion is defined as the work which is needed to separate the interface from the equilibrium state of two phase (liquid/solid) to a separation distance of infinity [36]. The work of adhesion is descirbed as Equation (6):

$$W_a = \gamma_L + \gamma_S - \gamma_{SL} \quad \text{(6)}$$

According to OWRK Equation (3), the work of adhesion can also be expressed by Equation (7):

$$W_a = 2(\sqrt{\gamma_l^d \gamma_s^d} + \sqrt{\gamma_l^p \gamma_s^p}) \quad \text{(7)}$$

The above equation is based on the known components and parameters of liquid and solid. If not, the work of ahesion can also be calculated by Young-Dupree Equation (8) [37]

$$W_a = \gamma_L(1+\cos\theta) \quad \text{(8)}$$

3. Results

3.1 3-Dimensional topography and surface roughness

Many of the previous reports [38-40], suggested that LSP increases the surface roughness with increasing laser energy and multiple impacts. In the meanwhile, surface topography and surface chemistry determine the wettability of materials. Therefore, studying the effect of LSP on the surface roughness is quite necessary. Both 2-D and 3-D topography of LSPned samples were mapped, and the cross-sectional profiles along the X and Y directions(as defined in figure 1) were presented in Figure 6. The average area surface roughness Sa (arithmetic mean of the absolute values of the surface departures from the mean plane) and Ra (arithmetical mean roughness value over the entire measured length, the cross lines as shown in figure 6) as a function of primary LSP parameters laser energy and spot overlap are given in Figure 5. Overall, in the longitudinal direction, it can be seen that increasing the laser energy will lead to the rise of surface roughness. At the same laser energy level, all three curves decrease with increasing spot overlapping rate. In particular, at the laser energy of 3J, the values of both Sa and Ra as a function of are nearly the same around 0.5-0.52μm for all overlaps tested. Excluding the lowest energy, 5J and 7J curves decline more significantly from 50% to 67% overlap, while in the range of 33% to 50% overlap, the reduction of surface roughness is much lower.

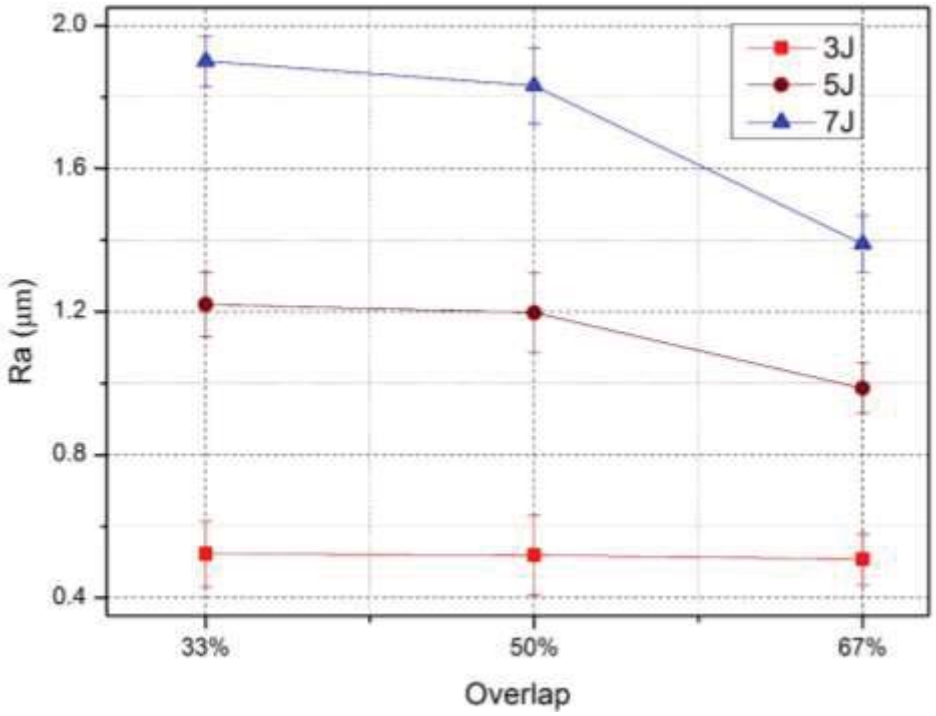

(a)

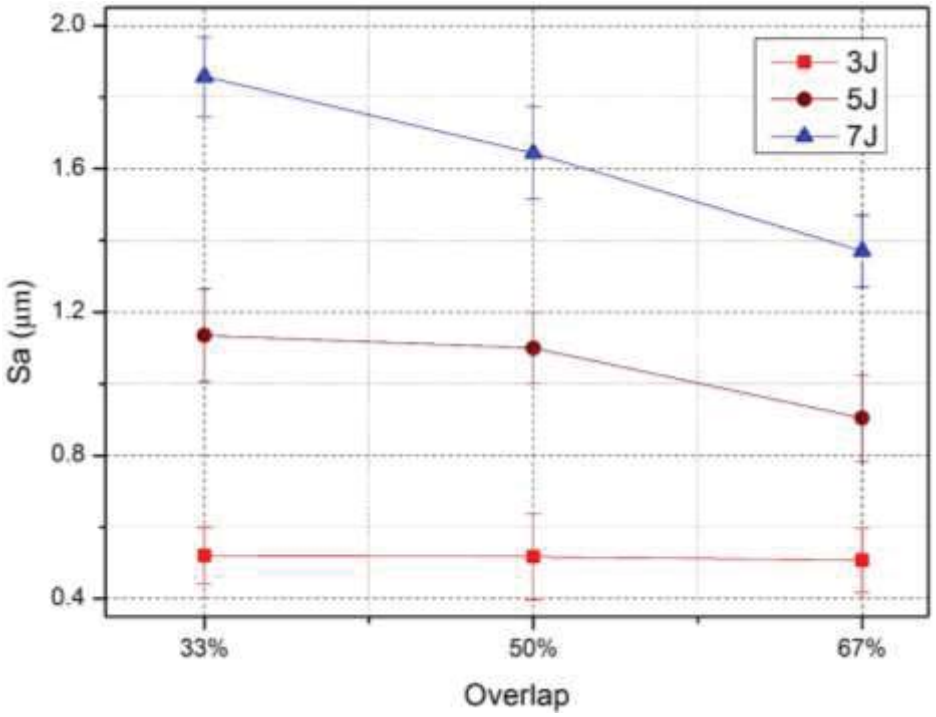

(b)

Figure 5 The distribution of Sa and Ra with overlap and laser energy.

By changing, LSP parameters such as laser energy, overlap, spot size, surface characteristics such as grooves and dimples can be acquired. According to grooves direction, each sample was placed along the longitudinal orientation (Y-direction). At the same overlay, the topographies are very similar but due to different energy the surface morphology is different.

As shown in figure 6(Surfa) and listed in table 3, in terms of 33%, due to the 2/3 step movement (33% overlap), comparatively large dimples are formed after LSP while grooves are not observed. In the 3J X profile, the upper asperity is 1μm and the deepest reaches to -1.5 μm, while the values at 5J and 7J are 1.8μm /-3μm and 2.1μm/-4μm. And for Y profile, the top is 1μm and bottom is at -1.2μm. while the values of 5J and 7J are 2μm/-3μm and 4μm/-4μm. Therefore, it can be concluded that the size of these dimples are proportional to laser energy at the 33% overlap. Compared to 33% overlap, a square-grid topography was formed on 50% overlap samples subject to LSP due the 1/2 step movement during the LSP processing. Additionally, grooves are formed upon the surfaces. In terms of amplitude of the curves, the highest among these samples is 2μm /-4μm (7J), then followed by 3.8 μm /-2 μm (5J), 1.5 μm /-1 μm (3J) in Y direction, while the sequence in X direction is 4 μm /-4 μm (7J), 3 μm /0 μm (5J) , 1.8 μm /-0.2 μm (3J). In the overlap of 67%, due to the smaller step movement (1/3), the width of the groove is much smaller than one of 33% (2μm) overlap and 50% (1.54μm) overlap with average distance of 1μm in X direction while in Y direction the values are 1 μm (7J), 1.54 μm (5J), 2.8 μm (3J). Regarding

to the amplitude, in X direction, they are 0.5 μm /-0.5 μm (3J), 2 μm /0 μm (5J), 4 μm /-1 μm (7J); and in Y-direction, they are 1 μm /-1 μm (3J), 1 μm /-2 μm (5J), 3.8 μm /0 μm (7J).

Table 3 Amplitude in X/Y profile of Laser Shock Peened samples

	33%(Highest/Lowest, μm)		50%(Highest/Lowest, μm)		67%(Highest/Lowest, μm)	
	X	Y	X	Y	X	Y
3J	1/-1.5	1/-1.2	1.8/-0.2	1.5/-1	0.5/-0.5	1/-1
5J	1.8/-3	2/-3	3/0	3.8/-2	2/0	1/-2
7J	2.1/-4	4/-4	4/-4	2/-4	4/-1	3.8/0

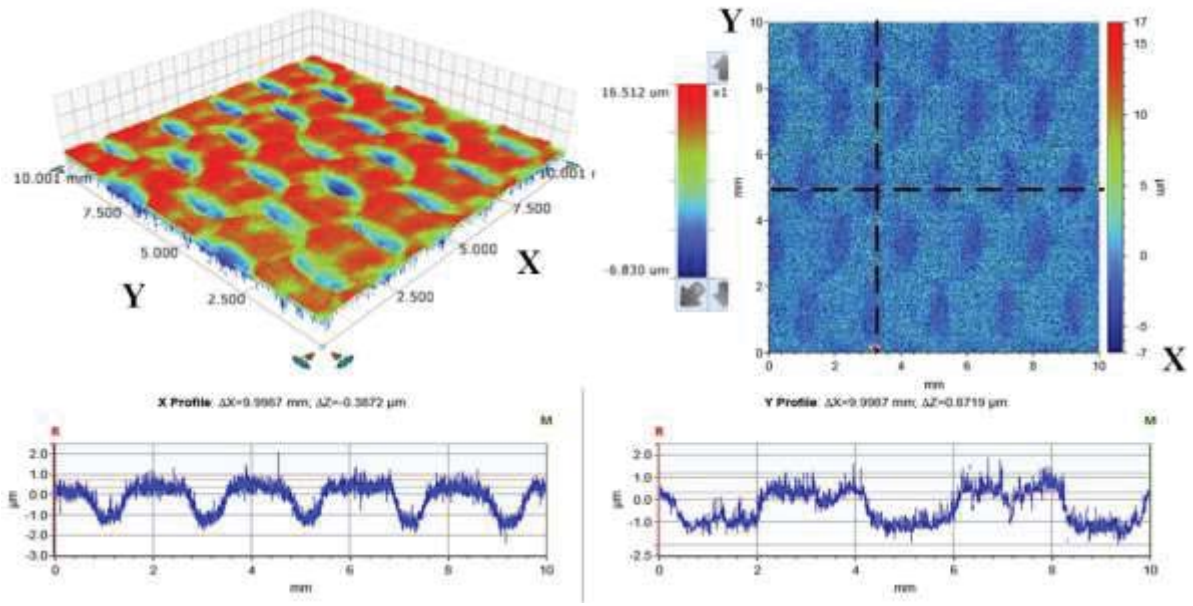

(a)

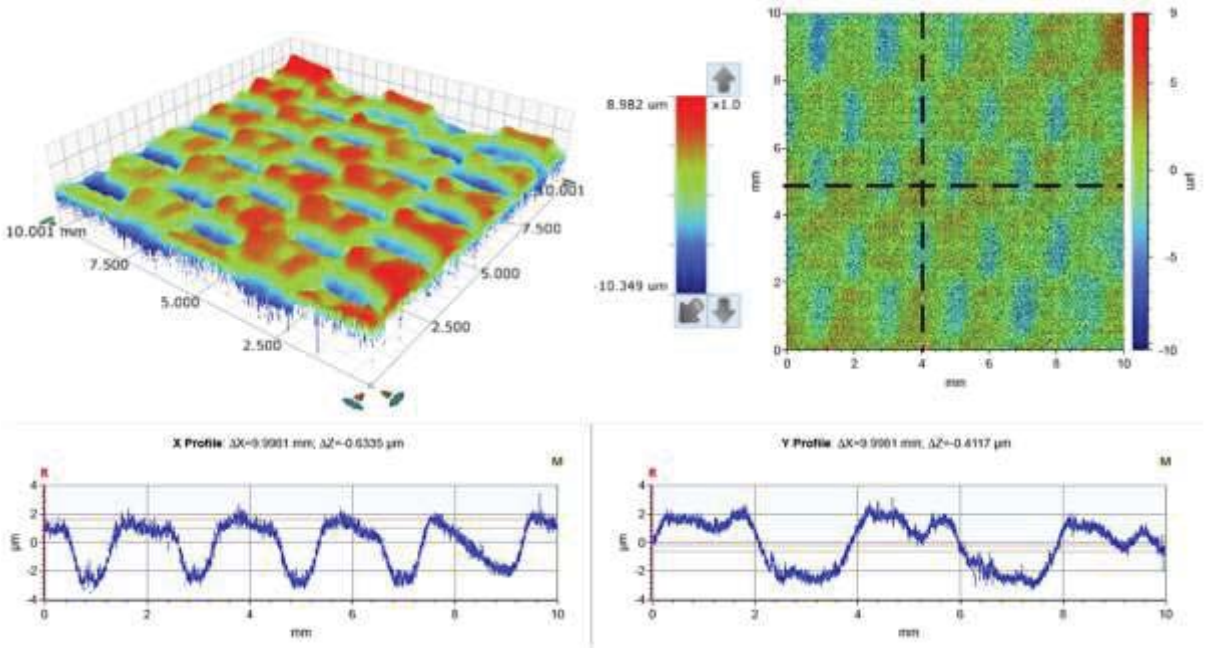

(b)

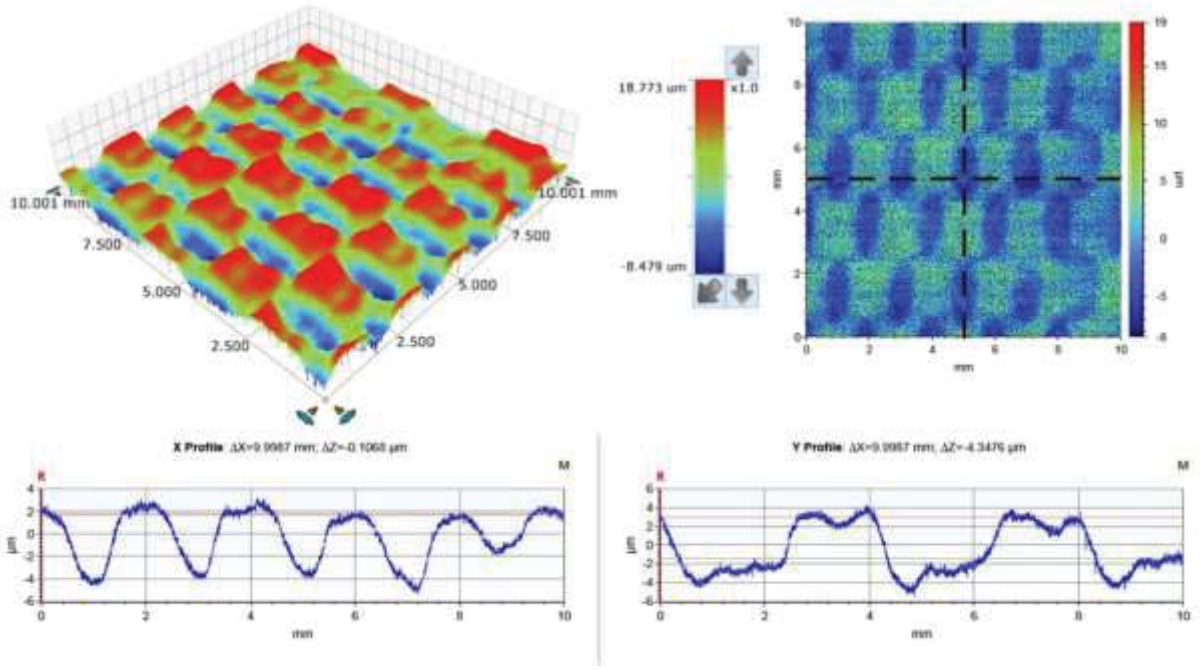
18.773 um
x1.0
-8.479 um
10.001 mm
7.500
5.000
2.500
mm
X Profile ΔX=9.9987 mm; ΔZ=-0.1068 µm
Y Profile ΔX=9.9987 mm; ΔZ=-4.3476 µm
µm

(c)

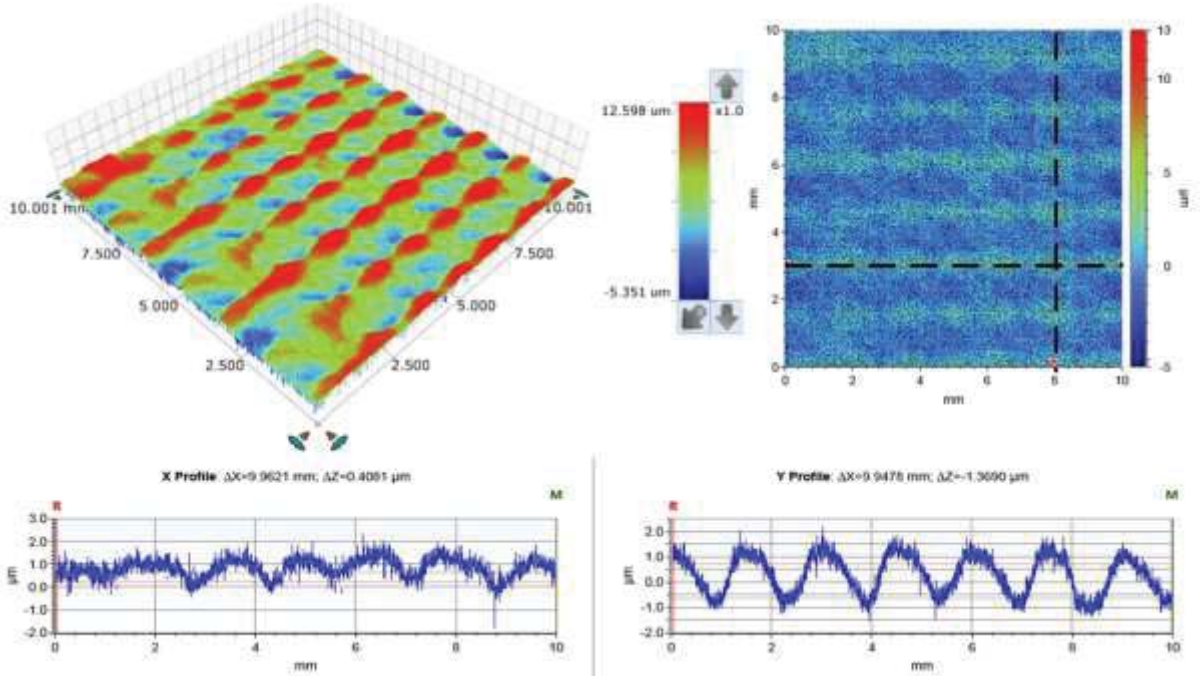
12.598 um
x1.0
-5.351 um
10.001 mm
7.500
5.000
2.500
mm
X Profile ΔX=9.9621 mm; ΔZ=0.4081 µm
Y Profile ΔX=9.9478 mm; ΔZ=-1.3690 µm
µm

(d)

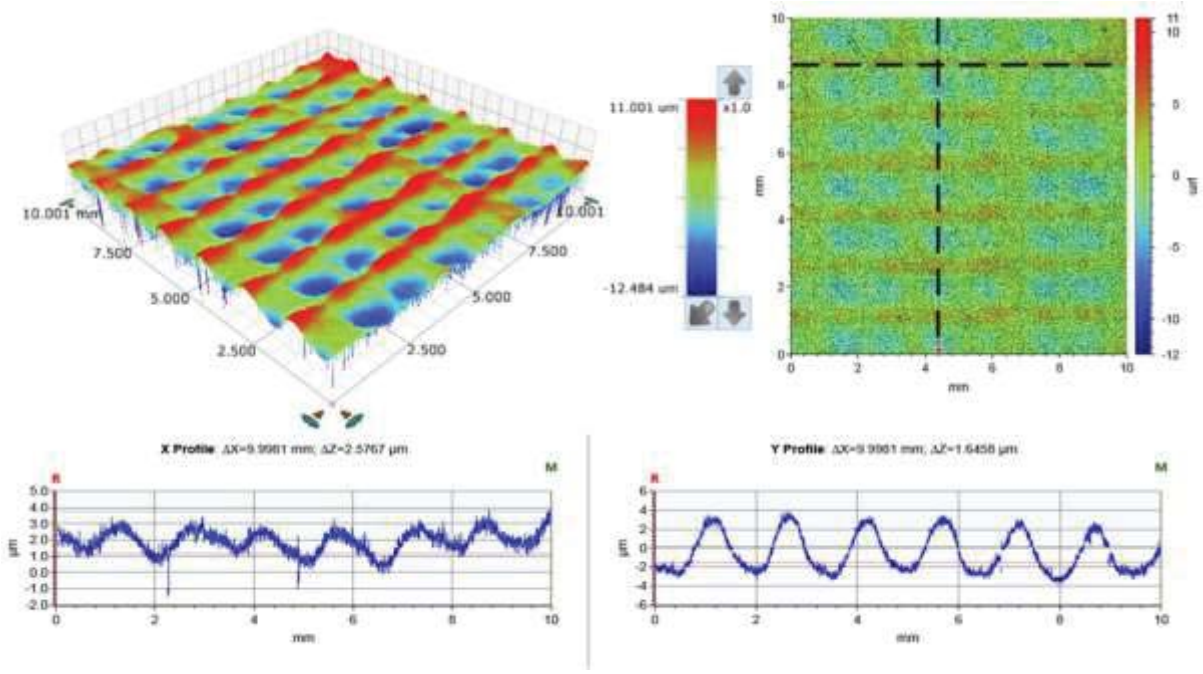
10.001 mm
7.500
5.000
2.500
11.001 um
x1.0
-12.484 um
mm
um
X Profile: ΔX=9.9981 mm; ΔZ=2.5767 µm
Y Profile: ΔX=9.9981 mm; ΔZ=1.6458 µm
µm
mm

(e)

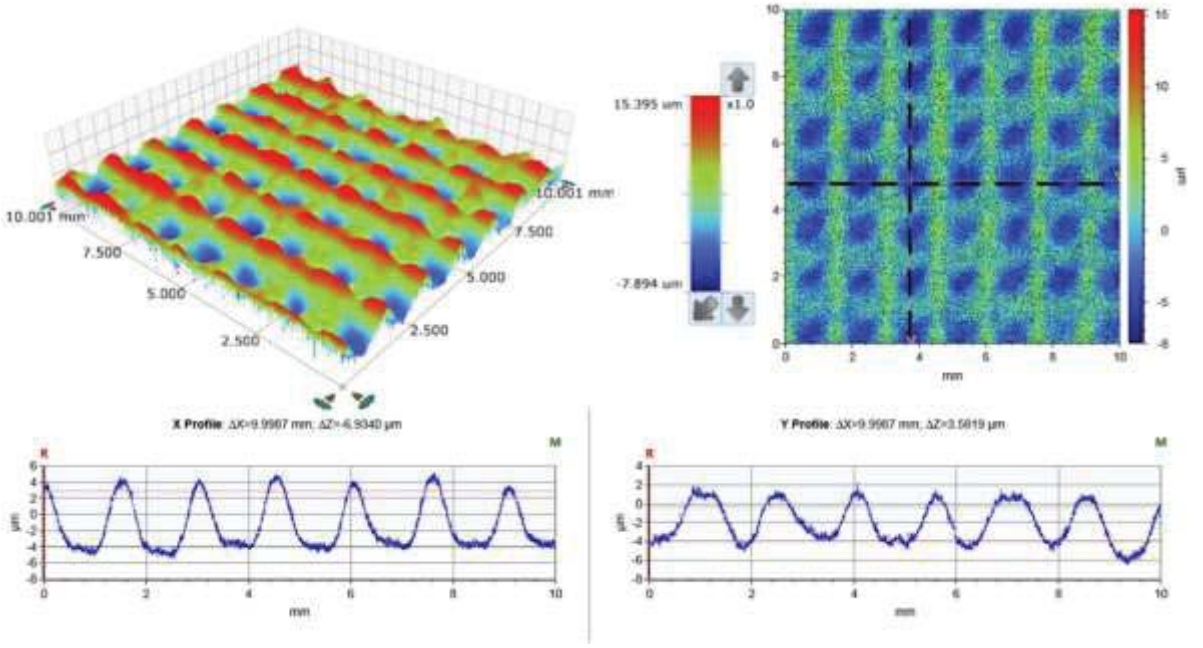
10.001 mm
7.500
5.000
2.500
15.395 um
x1.0
-7.894 um
mm
um
X Profile: ΔX=9.9967 mm; ΔZ=4.9340 µm
Y Profile: ΔX=9.9967 mm; ΔZ=3.5819 µm
µm
mm

(f)

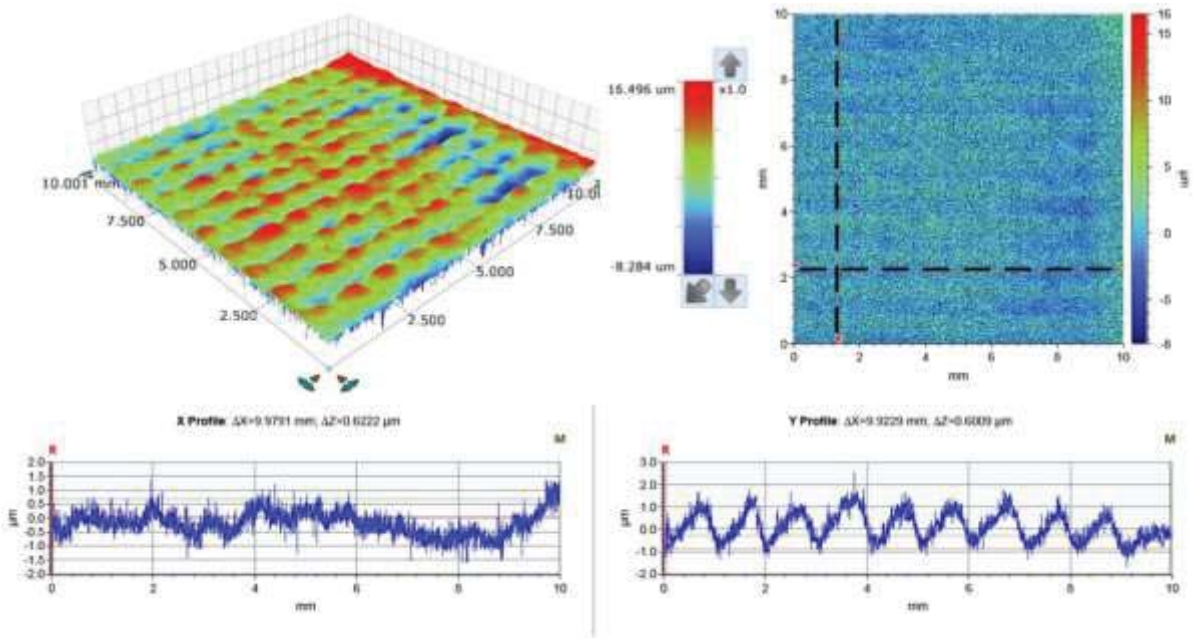
15.496 um
x1.0
-8.284 um
10.001 mm
7.500
5.000
2.500
mm
X Profile: ΔX=9.9791 mm; ΔZ=0.6222 µm
Y Profile: ΔX=9.9229 mm; ΔZ=0.6089 µm
µm

(g)

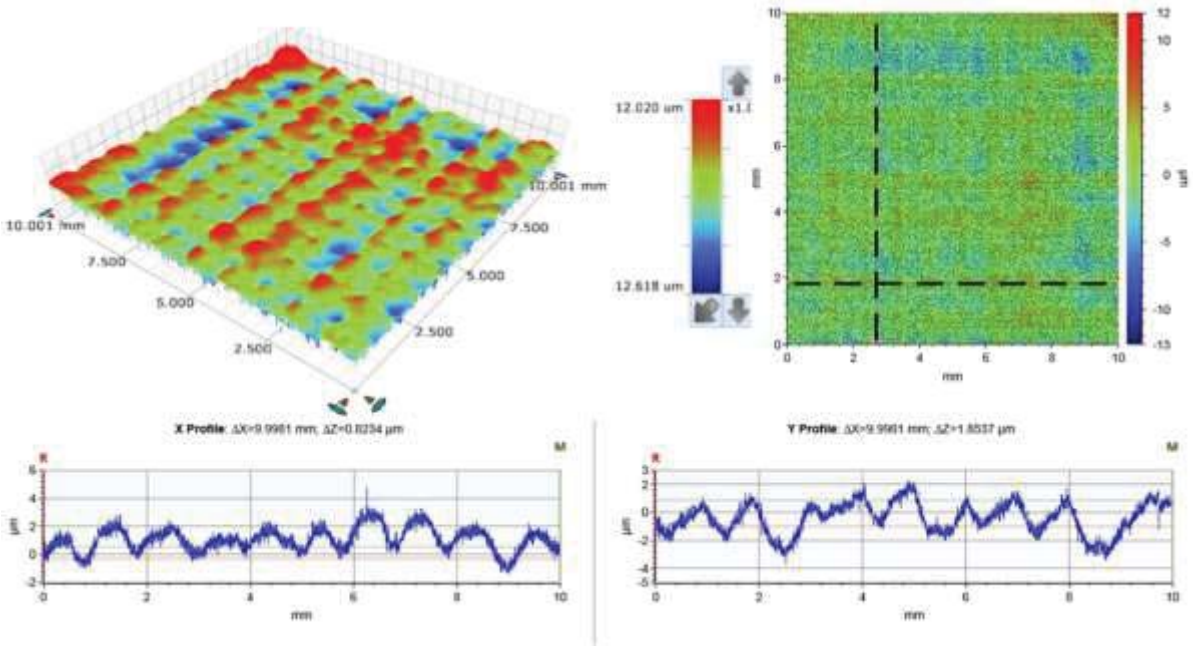
12.020 um
12.618 um
10.001 mm
7.500
5.000
2.500
mm
X Profile: ΔX=9.9961 mm; ΔZ=0.8234 µm
Y Profile: ΔX=9.9961 mm; ΔZ=1.8537 µm
µm

(h)

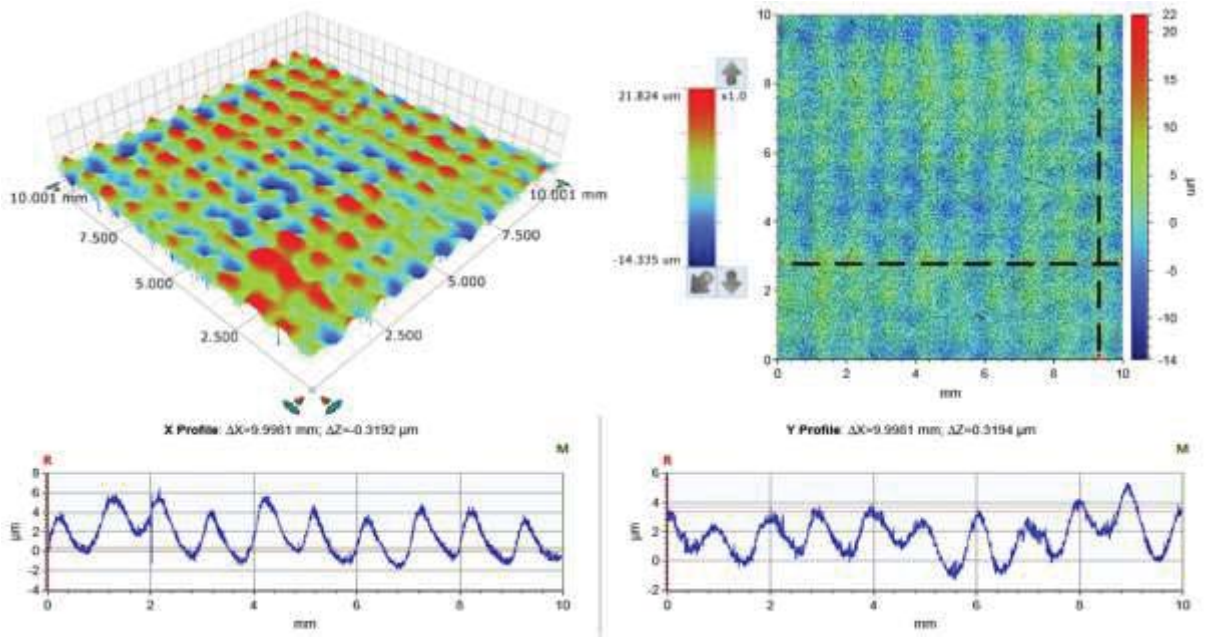

(i)

Figure 6 Surface topography images showing Laser Shock Peened Ti-6Al-7Nb samples for 33% @ 3J in (a), 33% @ 5J in (b), 33% @ 7J in (c); 50% @ 3J in (d) 50% @ 5J in (e); and 50% @ 7J (f); 67% @ 3J in (g), 67% @ 5J in (h) and 67% @ 7J in (i).

3.2 Residual Stress-Incremental hole drilling

Laser shock peening can introduce a stable compressive residual stress layer on the surface of metallic materials through high pressure shock-waves. The cross-section residual stress of full LSP parameters Ti-6Al-7Nb samples (including as-received), were measured by incremental hole drilling method as shown in Figure 7(a) and (b). The distribution of cross-sectional residual stress before and after LSP resulted to a stable compressive residual stress layer in both circumferential and axial directions. It can be seen that the sub-surface residual stress of the as-received sample was tensile (225MPa) on both axial and circumferential directions. However, after LSP, the sub-surface residual stresses are all modified into compressive, varying from -42MPa to -516 MPa. In the as-received residual stress curve, the line decreased from tensile 200 MPa to 0 MPa at the depth of about 175µm, then maintaining steadily at around 0 MPa, along the cross-sections. This tensile residual stress surface layer would be definitely harmful to the mechanical performance in terms of fatigue resistance. In terms of laser shock peened curves, for all samples on both directions, compressive affecting depths have been formed. These depths varied from 420µm (5J @ 33% overlap) to 1000 µm (5J @ 67% overlap). Some depth of laser shock peening could even be out of the range of measurement for instance at energy of 7J @ 67% overlap (residual stress reaches 0 MPa at a predicted depth of ~1500 µm). The difference in residuals stress magnitude occurred because the material deformation including dislocation movements caused by various laser energy and overlapping rate and with respect the difference in residuals stress direction , it would be quite small because the sample is circular. It is the magnitude of compressive residual stress depth that would most benefit mechanical properties of treated alloy.

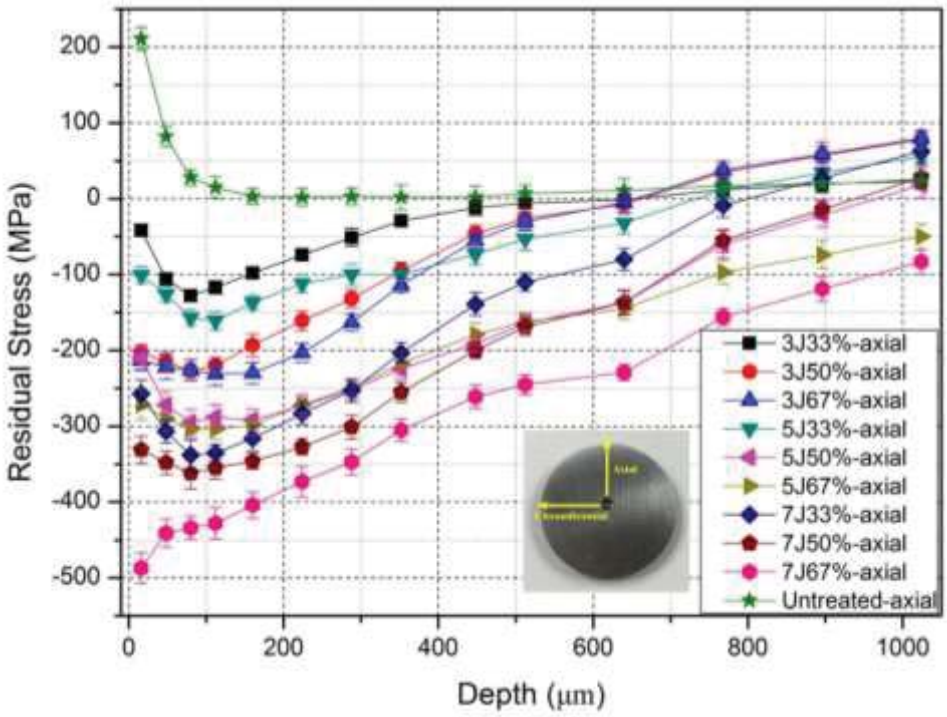

(a)

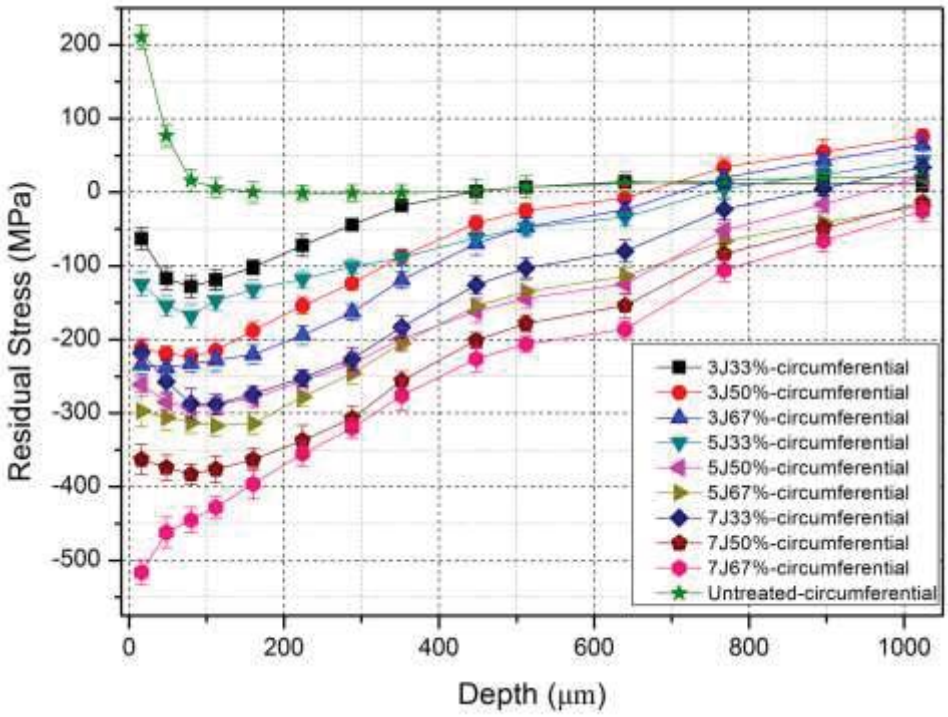

(b)

Figure 7 Cross-sectional distributions of residual stress of Ti-6Al-7Nb before and after LSP: (a) Axial direction, (b) Circumferential direction.

3.3 Microstructure observations and analysis

Figure 8 shows the SEM microstructure images of Ti-6Al-7Nb titanium alloy treated before and after laser shock peening (7J67%). As shown in figure 8(a)(b), it can be observed that Ti-6Al-7Nb titanium alloy consisted of globular coarse α-grain, acicular coarse α, and residual lamellar β grain. Increasing the magnification to x40K (fig.8(c)), the large globular α grain consisted of small α subgrains. Additionally, the grain boundaries of α subgrains are very clear. In order to calculate the average α subgrain size, the grain intercept method was employed. With that method, in the square of B (fig.8c), the average α subgrain size of untreated Ti-6Al-7Nb titanium along the cross-section is around 251 nm.

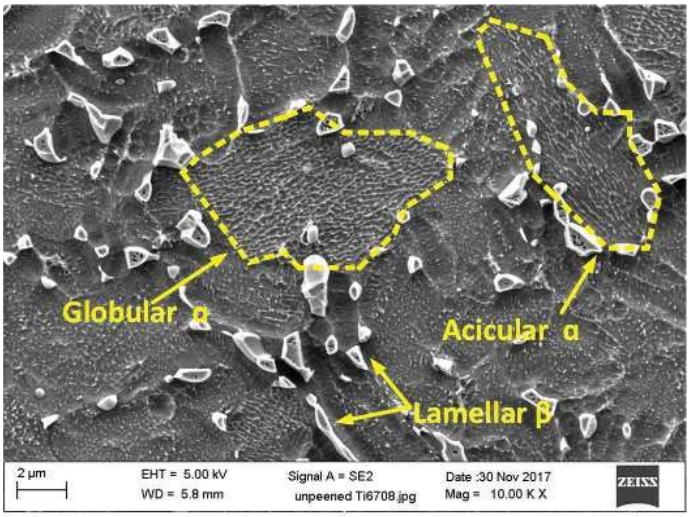

(a)

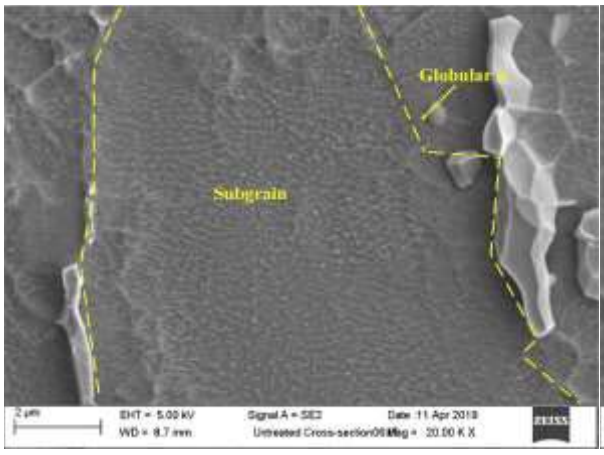

(b)

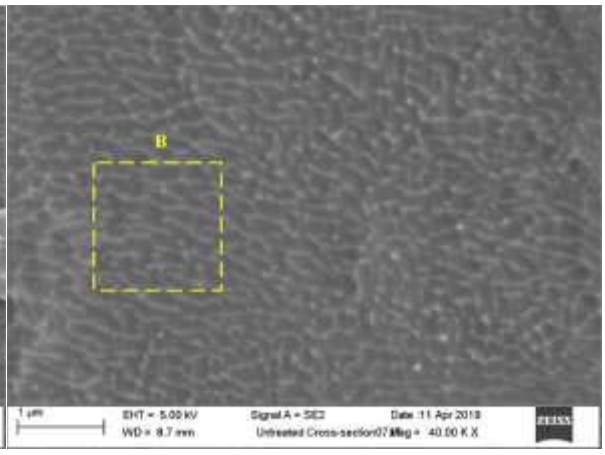

(c)

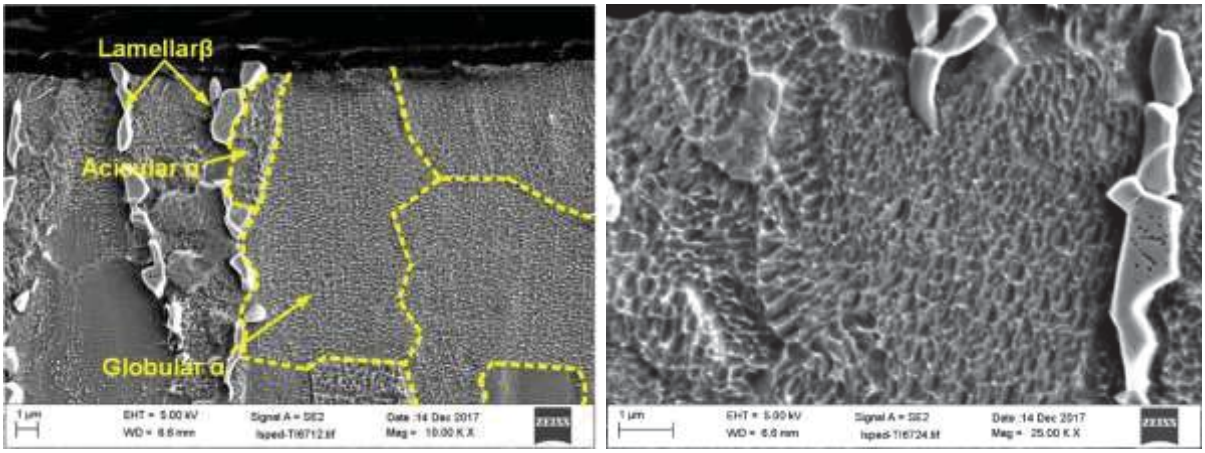

(d) (e)

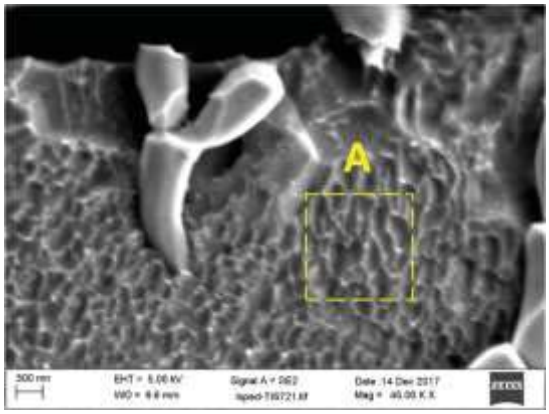

(f)

Figure 8: SEM images showing the surface and cross-sectional microstructures of the untreated and LSPned (7J67%) Ti-6Al-7Nb titanium alloy in (a) and (b) (c) at x10000, x20000, x40000 magnification, and the laser shock peened microstructures along the cross-section in (d), (e) and (f) at x10000, x25000 and x45000 magnification,

After LSP (7J67%), in Figure 8(d)-(f), the cross-section microstructure of Ti-6Al-7Nb titanium alloy is presented. In figure (d)-(f), no new phase has been observed post LSP. But, at the maginification of 45Kx, in the top-most area, the α subgrains appear further refined. By contast, the β-grains did not appear to receive any refinement from the laser shock wave from the SEM images. Using the intercept grain method, the LSPned average α subgrain size was 169 nm in square A of Figure 8(f) Therefore, by comparing the microstructure images of Ti-6Al-7Nb titanium alloy before and after LSP, the refinement of α subgrain is calculated to be 48.5%.

3.4 Wetting characterization

3.4.1 Contact angle and surface free energy

The dynamic advancing contact angle of Ti-6Al-7Nb alloy before and after LSP wetted with distilled water and ethylene glycol is presented in Figure 9 and table 4. For both Figures (9a) and (9b), the contact

angle curves are similar. As a base line, the contact angle of untreated samples with two liquids are separately 54.0 (distilled water) and 41.9(ethylene glycol). In comparison, all LSPned contact angles are higher than the untreated which correlates favourably with the work of Prabhakaran et al. [41] and Caralapatti et al. [42]. The highest water contact angle is 79.9°, and the ethylene glycol contact angle is 58.8, at the LSP condition of 3J@33% spot overlap. Meanwhile, the lowest water contact angle is 64.1°, and ethylene glycol contact angle is 47.1° which was generated under the LSP condition of 7J@67% spot overlap. What is more, observing the two figures from the longitudinal direction, contact angle values rise with the increase of laser energy at the same overlap. However, it is also apparent that the contact angles decreases with the increase of overlap at the same laser energy level.

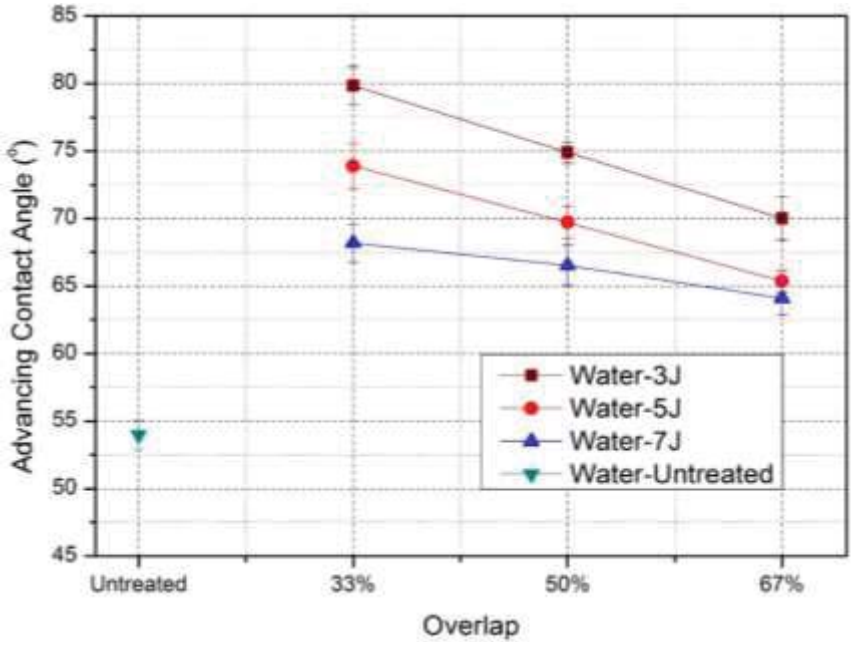

(a)

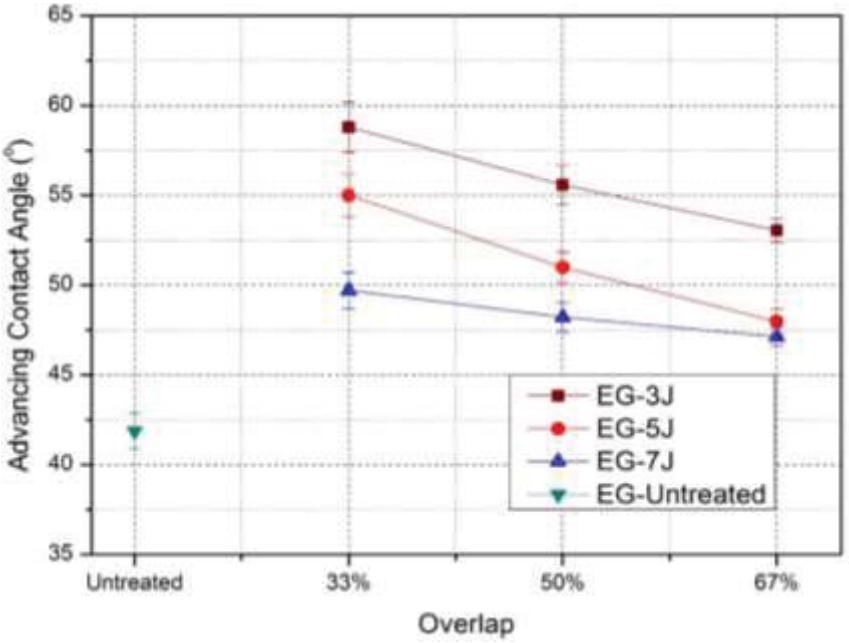

(b)

Figure 9 Advancing contact angle on both untreated and laser shock peened specimens for distilled water in (a) and ethylene glycol in (b).

Table 4 Advance contact angle for Ti-6Al-7Nb titanium alloy after laser shock peening.

	Distilled water			Ethylene glycol		
Overlap	3J	5J	7J	3J	5J	7J
33%	79.84	73.89	68.18	58.8	55	49.7
50%	74.91	69.71	66.52	55.58	50.99	48.22
67%	70.01	65.36	64.09	53.04	47.98	47.12
Untreated		53.96			41.87	

Calculated by using ORWK model with two different liquids (distilled water and ethylene glycol), the surface-free energy and its components is given in Table 5 and Figure 10.

Table 5 The surface-free energy and its components of Ti-6Al-7Nb post laser shock peening and untreated (units: mN/m.).

	$\gamma^T/(\gamma^d:\gamma^p)$							
Overlap	3J		5J		7J		Untreated	
33%	27.65		30.44		34.44		Untreated	47.68
	16.49	11.16	13.7	16.74	12.73	21.7		
50%	29.89		33.34		35.68			
	14.23	15.67	13.13	20.21	12.38	23.3		6.74:40.94
67%	32.87		36.55		37.58			
	11.55	21.32	11.47	25.08	10.99	26.59		

In terms of SFE, the highest value is obtained in untreated specimen with the value of 47.68mN/m. Among the LSPned samples, specimen 7J&67% reaches the highest surface energy (37.58 mN/m) while the lowest is specimen 3J 33% (27.65 mN/m). According to the Wenzel's theory [43], if the surface roughness is increased, the contact angle should be decreased. However, in real application, contact angle of specimen after LSP increases. This is because the surface free energy of the LSPned specimen are decreased due to laser ablation. (Normally, CA is inversely proportional to SFE). In the same overlap column, the SFE at 7J specimens are always the highest among their different laser energy, while the one of 3J is the lowest. Additionally, at the same laser energy level, SFE has a positive correlation with the overlap. What interesting is that the SFE difference among three laser energies become smaller when the overlap increases from 33% to 67%.

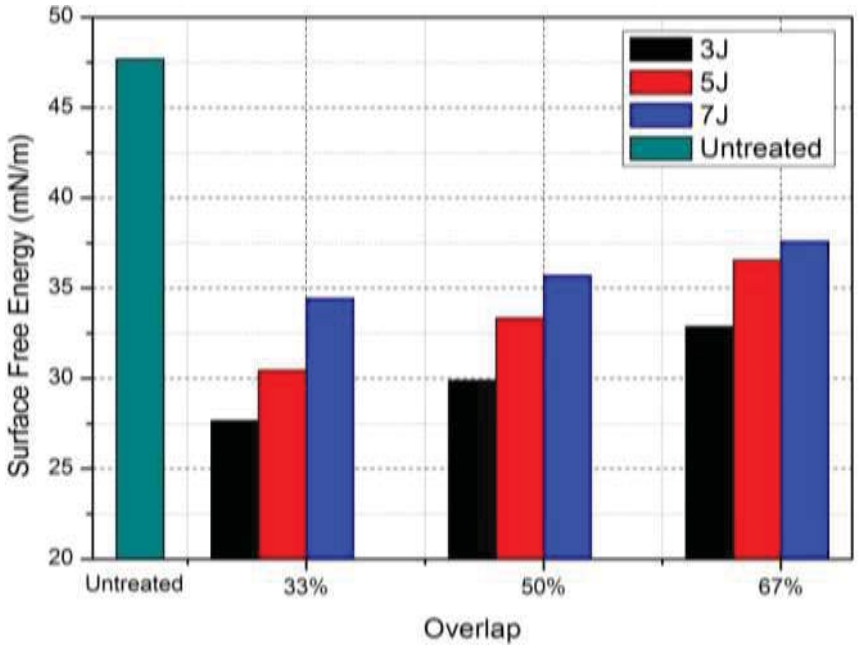
Surface Free Energy (mN/m)
50
45
40
35
30
25
20
3J
5J
7J
Untreated
Untreated
33%
50%
67%
Overlap

(a)

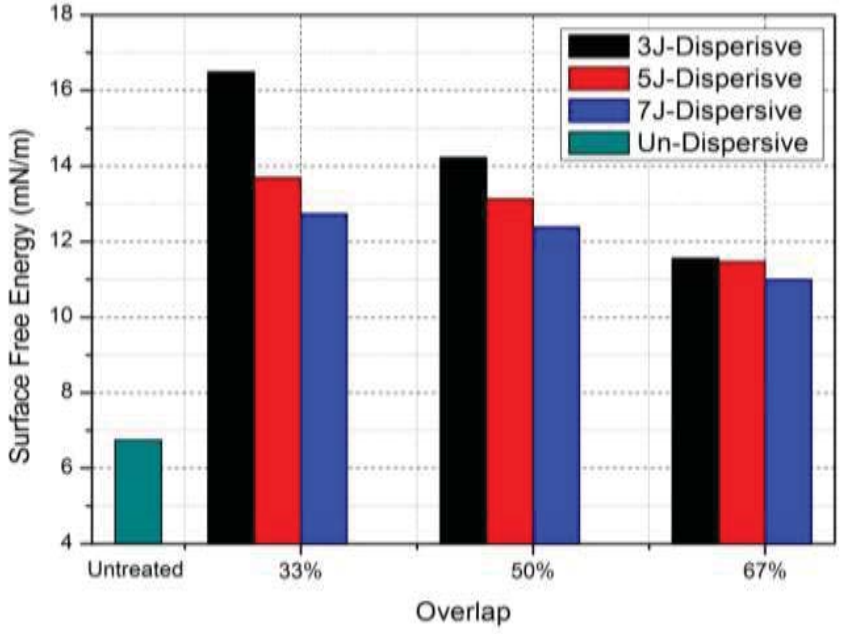
Surface Free Energy (mN/m)
18
16
14
12
10
8
6
4
3J-Disperisve
5J-Disperisve
7J-Dispersive
Un-Dispersive
Untreated
33%
50%
67%
Overlap

(b)

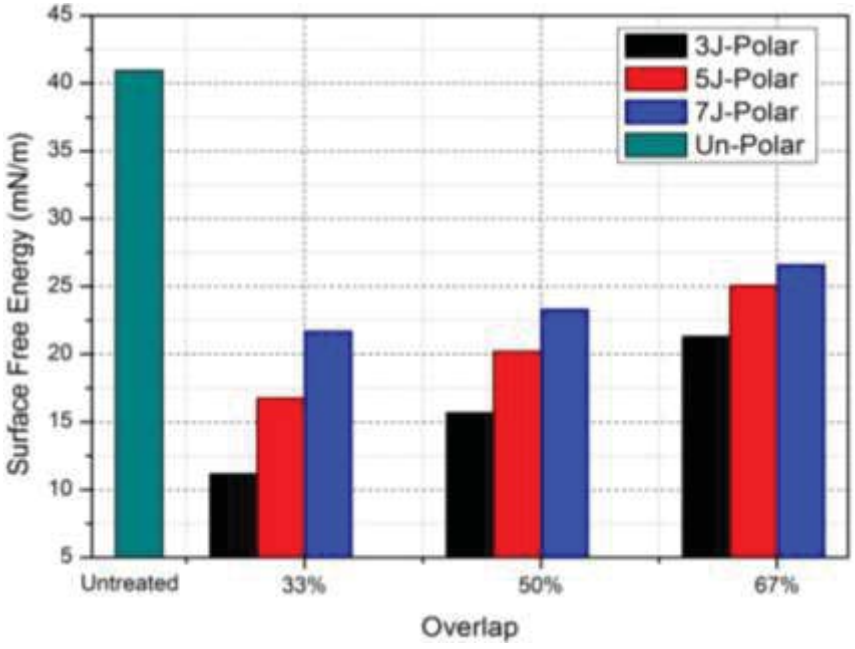

(c)

Figure 10 The surface free energy (a) , and its components dispersive(b) and polar(c).

Figure 10 (b) and (c) exhibit the distribution of dispersive component and polar component of SFE from Ti-6Al-7Nb alloy. It can be seen that the 40.94mN/m out of 47.68mN/m is polar component, and dispersive part is 6.74mN/m. The polar part account for 85.78% in the total SFE. However, after LSPned, the ratio has been dramatically changed. In Figure 10(c), the polar columns have the similar tendency as the total SFE columns(Fig10a) With regard to dispersive component distribution, all dispersive component of SFE LSPned samples are higher than that of untreated one. It is evident from Fig 10b that the highest value of the dispersive component is attained at the LSP condition 3J_33% overlap; Increasing overlaps (@3J) causing a reduction in the dispersive component of SFE. This trend is mirrored by samples treated at higher peening energies and overlaps, although the effect of peeing energy on the dispersive component reduces with increasing overlap.

3.4.2 Work of adhesion

The adhesion work of Ti-6Al-7Nb specimens for wetting liquids (distilled water and ethylene glycol), calculated from equation (ORWK), is given in Figure 11 (a) and (b) and Table 6. For both liquids, the highest Wa is produced in the untreated specimen (Distilled water:115.63mN/m; Ethylene glycol:83.743mN/m). The adhesion work at 7J is higher than others laser peened samples with the same overlap. With the same laser energy, the adhesion work rises moderately with the increase of overlap for both wetting liquids. What is more, when the wetting fluid is distilled water, on the 7J specimens, the difference is quite small with the value of 4.75º, while the one of 3J specimens is 12.05º. Using ethylene glycol, such values are 1.62 º(7J) and 4 º(3J).

Table 6 The work of adhesion of distilled water and ethylene glycol on the LSPned specimens(J/m^2).

	Distilled water			Ethylene glycol		
	3J	5J	7J	3J	5J	7J
30%	85.64	93.00	99.86	72.87	75.53	79.05
50%	91.75	98.04	101.81	75.13	78.21	79.98
67%	97.69	103.15	104.61	76.86	80.13	80.66
	Distilled water			Ethylene glycol		
Untreated	115.63			83.74		

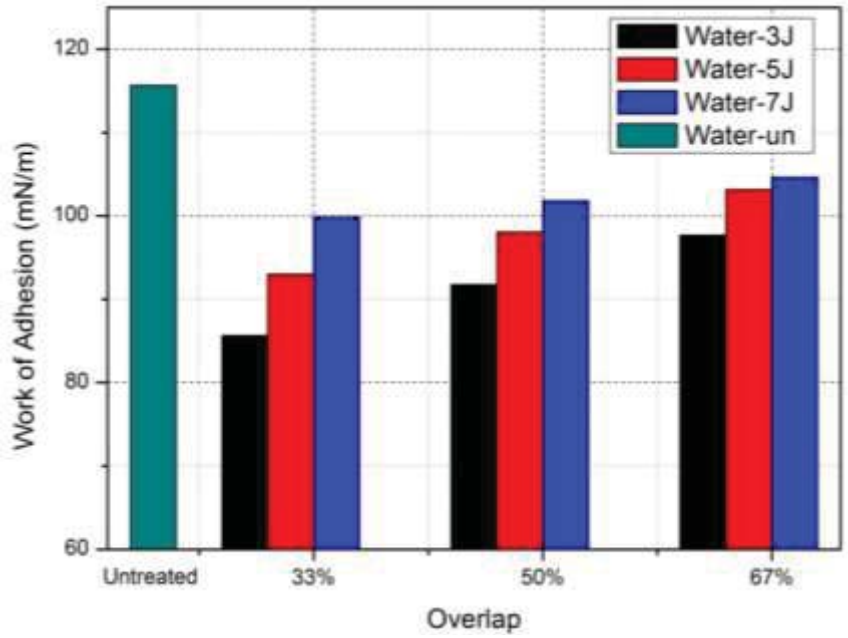

(a)

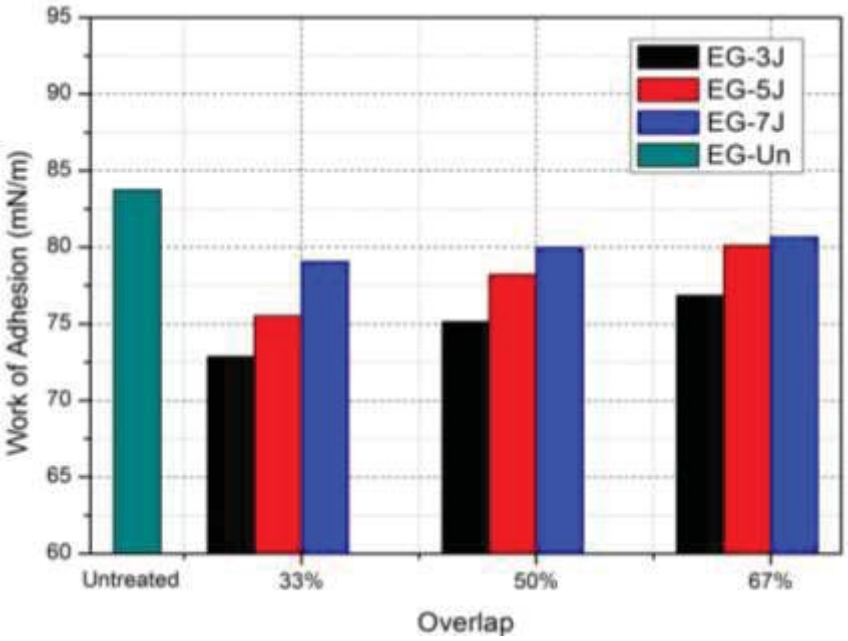

(b)

Figure 11 Work of adhesion of distilled water in (a) and ethylene glycol in (b) onto the LSPned and untreated specimen surface.

4. Discussion

As mentioned in previously, the wettability of a substrate by a fluid is determined by surface topography and surface physic-chemistry properties [44]. In terms of chemical changes, it is common knowledge in the field that LSP applied under the conventional conditions (water confinement and black polyvinyl ablative layer) will not induce any change in surface chemistry. However, the surface topography and surface grain refinement introduced by LSP will naturally affect the wettability of materials. What is more, due to titanium`s high affinity for oxygen, a thin oxide layer, mainly consisted of TiO_2, Ti_2O_3, and TiO, is immediately formed when titanium is exposed to air. The thickness of the film will increase with the time according to environmental conditions. With the isolation from the substrate by TiO_x, the contact angle of wetting liquid is determined by both oxide layer and the refined surface microstructure. Researches [45, 46] have confirmed that the surface-free energy of an ultrafine surface is higher than that of a coarse grain material in titanium alloys with thin a TiOx layer. In previous section 3.3, the surface microstructure before and after LSP show that average surface grain is refined from 267nm to 150 nm which is one of source of the evidence of the improvement of the surface-free energy post LSP. What is more, surface roughness and surface topography also play a fundamental role in the wetting behaviour. As mentioned above, Wenzel introduce a surface roughness factor *r* into to Young's equation showing in the following equation.

$$\cos\theta_W = r(\gamma_{SG} + \gamma_{SL}) / \gamma_{LG} = r\cos\theta_Y \tag{9}$$

Where *r* is the surface roughness factor; the equation describes the mechanism that roughness can enhance the wetting behaviour of the solid surface. In another case, Cassie-Baxter further considered the material surface is randomly consists of n pieces of small materials. Additionally, every piece of material is characterized by the factor of surface characteristics, namely, surface tension or surface energy i.e. the Cassie-Baxter Equation is expressed as follow:

$$\cos\theta_{CB} = \sum_i^n f_i(\gamma_{i,SV} - \gamma_{i,SL}) / \gamma_{LV} = \sum_i^n f_i \cos\theta_{i,Y} \quad \text{.....(10)}$$

Where $\gamma_{i,SV}$ and $\gamma_{i,SL}$ is the surface energy/tension of each piece material. And f_i is the respective material fraction with $f_1 + f_2 + ... + f_n = 1$. It should be noted that in some specific application, both regimes can coexist on the same surface. The schematic diagram of Wenzel`s model and Cassie-Baxter Model is showed in Figure 12.

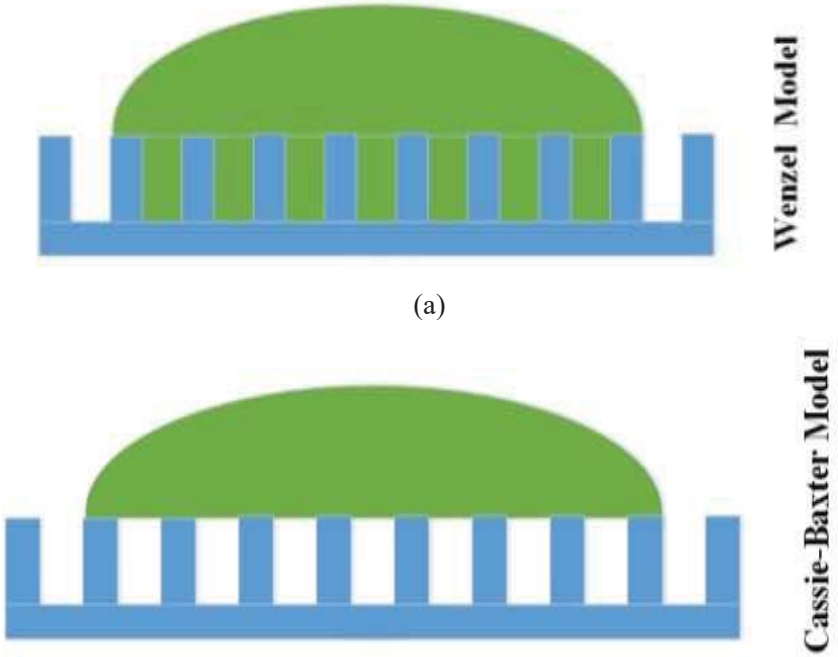

Figure 12 The schematic images showing the Wenzel Model in (a), and Cassie-Baxter Model in (b).

In the case of LSPned specimens, obviously, the mechanism is not determined by Wenzel regime, while it should be the Cassie-Baxter or the combination model. In Figure 13, the relationship between surface roughness and surface-free energy is shown. At the same laser energy level, rougher surface facilitate a reduction in SFE. Additionally, compared to 7J specimens, the curve of 3J is steeper, nearly vertical to the surface axis.

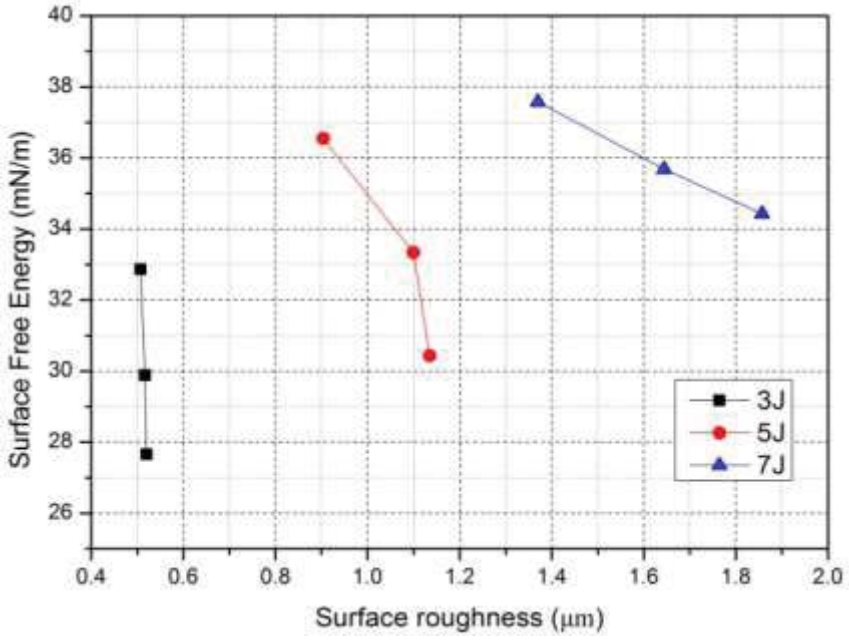

Figure 13: The distribution map showing the Surface-Free Energy with average surface roughness (Sa).

To explain why the contact angle of 7J specimen is higher than the ones of 3J and 5J specimens in the same overlap, the following statement is presented. With consistent spot overlap and laser energy as a variable, the surface morphology remains consistent showed in the 3D and 2D images in section 3.1. In particular, the shape of surface characteristics namely grooves and dimples are same. The difference among the surface morphologies is the specific topography of the groove and dimple introduced by variable laser energy. Compared to an ideal surface, when a liquid drop sits onto such grooves and dimples, according to Wenzel, The defects (grooves and dimples) on the surfaces will be filled by the wetting liquid. Thus, the volumetric quantity of liquid is lower than same volumetric quantity on top of a flat surface. The mechanism presented above can be explained by Wenzel's model which suggests that the higher the surface roughness, the lower contact angles. However, it can be only applied among the specimens subject to laser shock peening.

Furthermore, when the laser energy is kept consistent, with overlap as a variable, the contact angle is proportional to overlap (surface roughness). Therefore, in this case, the Wenzel's model is not suitable while Cassie-Baxter model or the combination of both may well be better suited.

5. Conclusions

This work has shown that despite laser shock peening (LSP) widely known as a technique to enhance fatigue resistance of metallic materials, the technique could also modify the wettability of solid metallic surfaces. The other benefit of this process is that it does not introduce new chemical changes to the metallic surface with the conventional process set-up as used herein. The specific conclusions can be made as follows：

1） By different combination of laser energy and overlap applied *via* LSP, different surface morphologies can be generated. The surface roughness rises with an increase of laser energy. By applying consistent overlapping and laser energy, the surface roughness separately has positive and negative correlation with surface-free energy;

2） In the sub-surface, the residual stress of as-received sample was tensile 200 MPa. Post LSP, compressive residual stress of -41MPa to -516 MPa were formed from the various laser energy and overlaps applied. These compressive residual stresses subsequently decreased with increasing depth and at the depths of 600μm to 1000μm, decreased to 0 MPa. At the highest laser energy and extents of overlap, moderate compressive residual stresses were still present at depths greater than 1000μm;

3） It was observed that an increase in overlap leads to a decrease in contact angle at the same laser energy level and increasing the laser energy has a negative correlation with contact angle when applying it at the same overlap. Due to the negative correlation to contact angle, the surface-free energy, and work of adhesion has an opposite correlation with laser energy and the overlap. It should be noted that with the increase overlap, the overall dispersive component decreases while the polar part of surface-free energy increases.

4） In untreated and LSPned specimens, the reduction of surface-free energy is used to address why the contact angle is improved after LSP. Comparing the contact angle of variable laser energy at the

same overlap, the main mechanism can be explained by Wenzel's model. Additionally, the effect of overlap at the same laser energy can be explained with the Cassies-Baxter model as the increase surface roughness leads to an inversely proportional increase in Contact angle.

Overall, LSP is used to reduce the surface-free energy by applying variable laser energy. Furthermore, adjusting the ratio of dispersive and polar components can be fulfilled by changing the overlapping during the LSP process.

6. References

[1]. Qian Ye, Guo He, In-situ formed graded microporous structure in titanium alloys and its effect on the mechanical properties [J], Materials & Design, 83(2015) 295-300.

[2]. C.P.W. Hammann, C.Th.H. Heerkens, C.W. Hagen, A.A. Zadpoor, L.E. Fratila-Apachitei, Direct submicron patterning of titanium for bone implants [J], Microelectronic Engineering, 195 (2018) 13-20.

[3]. Y. Torres, P. Trueba, J.J. Pavon, E. Chicardi, P. Kamm, F. Garcia-Moreno, J.A. Rodriguez-Ortiz, Design, processing and characterization of titanium with radial graded porosity for bone implants [J], Materials&Design, 110(2016) 179-187.

[4]. William J. Long, MD, FRCSC, Samir Nayyar, MD, Kevin K. Chen, MA, David Novikov, BS, Roy I. Davidovitch, MD, Jonathan M. Vigdorchik, MD, Early aseptic loosening of the tritanium primary acetabular component with screw fixation [J], Arthroplasty Today, 4 (2018) 169-174.

[5]. Kensuke Igarashi, Kelvin I. Afrashtehfar, Clinical assessment of fractured implant abutment screws: the bernese silicone replica technique [J], The Journal of Prosthetic Dentistry, 119(2018) 717-719.

[6]. O. Comakli, M. Yazici, T. Yetim, A.F. Yetim, A. Celik, Effect of Ti amount on wear and corrosion properties of Ti-doped Al2O3 nanocomposite ceramic coated CP titanium implant material [J], Ceramics International, 44(2018) 7421-7428.

[7]. Min Ho Kwon, Hong Shik Shin, Chong Nam Chu, Fabrication of a super-hydrophobic surface

on metal using laser ablation and electrodeposition [J], Applied Surface Science, 288(2014) 222-228.

[8]. M. Edalatpour, L. Liu, A.M. Jacobi, K.F. Eid, A.D. Sommers, Managing water on heat transfer surfaces: A critical review of techniques to modift surface wettability for applications with condensation or evaporation [J], Applied Energy, 222(2018) 967-992.

[9]. Qifeng Du, Jianguo Liu, Lianbo Guo, Ming Lv, Xiaoyan Zeng, Tailoring the surface wettability of polyimide by UV laser direct texturing in different gas atmospheres [J], Material&Design, 104(2016) 134-140.

[10]. Jan M. Macak, Hiroaki Tsuchiya, Luciano Taveira, Andrei Ghicov, Patrik Schmuki. Self-organized nanotubular oxide layers on Ti-6Al-7Nb and Ti-6Al-4V formed by anodization in NH4F solutions[J],Journal of Biomedical Research, 75A(2005)928-933.

[11]. Eugeniu Balaur, Jan M.Macak, Hiroaki Tsuchiya, Patrik Schmuki. Wetting behaviour of layers of TiO_2 Nanotubes with different diameters[J]. Journal of Materials Chemistry, 15(2005) 4488-4491

[12]. Molly M. Gentleman, Eileen Gentleman, The role of surface free energy in osteoblast-biomaterial interactions [J], International Materials Reviews, 59:8(2014) 417-429.

[13]. Thomas Groth, George Altankov, Studies on cell-biomaterial interaction: role of tyrosine phosphorylation during fibroblast spreading on surfaces varying in wettability [J], Biomaterials 17(1996) 1227-1234.

[14]. Lucas F.M. da Silva, N. M. A. J. Ferreira, V. Richter-Trummer, E.A.S.Marques, Effect of grooves on the strength of adhesively bonded joints[J], International Journal of Adhesion&Adhesives, 30(2010) 735-743.

[15]. C. Wang, X.J. Shen, Z.B. An, L.C. Zhou, Y. Chai, Effects of laser shock processing on microstructure and mechanical properties of K403 nickel-alloy [J], Materials&Design, 89(2016) 582-588.

[16]. Pratik Shukla, Subhasisa Nath, Guanjun Wang, Xiaojun Shen, Jonathan Lawrence, Surface property modifications of silicon carbide ceramic following laser shock peening [J], Journal of the European Ceramic Society, 37(2017) 3027-3038.

[17]. P. Shukla, S.Robertson, H. Wu, A Telang, M. Kattoura, S. Nath , S.R. Mannava, V.K. Vasudevan, J. Lawrence, Surface engineering alumina armour ceramics with laser shock peening [J], Materials & Design, 134(2017) 523-538.

[18]. Sihai Luo, Weifeng He, Kai chen, Xiangfan Nie, Liucheng Zhou, Yiming Li, Regain the fatigue strength of laser additive manufactured Ti alloy via laser shock peening [J], Journal of Alloys and Compounds, 750(2018) 626-635.

[19]. Mao-Zhong Ge, Jian-Yn Xiang, Yang Tang, X. Ye, Z Fan, Y.L. Lu, X.H. Zhang, Wear behavior of Mg-3Al-1Zn alloy subjected to laser shock peening [J], Surface and Coatings Technology, 337(2018) 501-509.

[20]. J.T. Wang, Y.K. Zhang, J.F. Chen, J.Y. Zhou, M.Z. Ge, Y.L. Lu, X.L. Li, Effects of laser shock peening on stress corrosion behavior of 7075 aluminum alloy laser welded joints [J], Materials Science and Engineering: A, 647(2015) 7-14.

[21]. S.R. Mannava, Sagar Bhamare, Vibhor Chaswal, Leonora Felon, David Kirschman, David Lahrman, Richard Tenaglia, Dong Qian, Vijay Vasudevan, Application of laser shock peening for spinal implant rods [J], International Journal of Structural Integrity, 2(2011) 101-113.

[22]. Vinodh Krishna Caralapatti, Sivakumar Narayanswamy, Effect of high repetition laser shock peening on biocompatibility and corrosion resistance of magnesium[J], Optics&Laser Technology, 88(2017) 75-84.

[23]. Yuebin Guo, Michael P Sealy, Changsheng Guo, Significant improvement of corrosion resistance of biodegradable metallic implants processed by laser shock peening [J], CIRP

Annals-Manufacturing Technology, 62(2012) 583-586.
[24]. M.P. Sealy, Y.B Guo, R.C. Caslaru, J. Sharkins, D. Feldman. Fatigue performance of biodegradable magnesium-calcium alloy processed by laser shock peening for orthopedic implants [J], International Journal of Fatigue 82(2016) 428-436.
[25]. Ruixia Zhang, Xianfeng zhou, Hongyu Gao, Steven Mankoci, Yang Liu, Xiahan Sang, Haifeng Qin, Xiaoning Hou, Zhencheng Ren, Gary L. Doll, Ashlie Martini, Yalin Dong, Nita Sahai, Chang Ye, The effects of laser shock peening on the mechanical properties and biomedical behavior of AZ31 magnesium alloy [J], Surface& Coatings Technology, 339(2018) 48-56.
[26]. Xiaojun Shen, Pratik Shukla, Subhasisa Nath, Jonathan, Lawrence, Improvement in mechanical properties of titanium alloy (Ti-6Al-7Nb) subject to multiple laser shock peening [J], 327(2017) 101-109.
[27]. Shukla, P., Lawrence J., Zhang, Yu. Understanding Laser-beam brightness: A Review on a New Prospective in Materials Processing, Optics and Lasers in Engineering, 75(2015), 40 – 51.
[28]. Shukla P.P., Lawrence, J. The influence of Brightness whilst Laser Surface Processing of a Silicon Nitride Engineering Ceramic, Optics and Lasers in Engineering, 50(2012), 1746-1751
[29]. Shukla, P.P., Lawrence, J. Role of laser beam radiance in different ceramic processing: A two wavelength comparison. Optics and Laser Technology, 54(2013), 380 – 388.
[30]. E.G. Orlova, D.V. Feoktistov, G.V. Kuznetsov, K.O. Ponomarev, Spreading of a distilled water droplet over polished and laser-treated aluminium surfaces [J], European Journal of Mechanics/B Fluids, 68 (2018) 118-127.
[31]. Zhang Shi, Yi Zhang, Mingchao Liu, Dorian A.H. Hanaor, Yixiang Gan, Dynamic contact angle hysteresis in liquid bridges [J], Colloids and Surfaces A: Physicochemical and Engineering Aspects, 555(2018) 365-371.
[32]. M. Zenkiewicz, Methods for the calculation of surface free energy of solids [J], Journal of Achievements in Materials and Manufacturing Engineering, 24(2007).
[33]. Anna Rudawska, Elzbieta Jacniacka, Analysis for determining surface free energy uncertainty by the Owen-Wendt method [J], International Journal of Adhesion and Adhesives, 29(2009) 451-457.
[34]. Peter C. Rieke, Application of Van Oss-Chaudhury-Good theory of wettability to interpretation of interfacial free energies of heterogeneous nucleation [J], Journal of Crystal Growth, 182(1997) 472-484.
[35]. David Garreth Waugh, Jonathan Lawrence, On the use of CO2 laser induced surface patterns to modify the wettability of poly(methyl methacrylate) (PMMA) [J], Optics and Lasers in Engineering, 48 (2010) 707-715.
[36]. Sina Ebnesajjad, Cyrus Ebnesajjad, Surface Treatment of Materials for Adhesive Bonding [M], William Andrew Press, 2013.
[37]. Malcolm E. Schrader, Young-Dupre revisited [J], Langmuir, 11(1995) 3585-3589.
[38]. Fengze Dai, Jianzhong Zhou, Jinzhong Lu, Xinmin Luo, A technique to decrease surface roughness in overlapping laser shock peening [J], Applied Surface Science, 370(2016) 501-507.
[39]. Luca Petan, Jose Luis Ocana, Janez Grum, Influence of laser shock peening pulse density and spot size on the surface integrity of X2NiCoMo18-9-5 maraging steel [J], Surface&Coatings Technology, 307(2016) 262-270.
[40]. Zhu Ran, Zhang Yongkang, Sun Guifang, Shen Xuting, Li Pu, Finite element analysis of surface roughness generated by multiple laser shock peening [J], Rare Metal Materials and Engineering, 47(2018)0033-0038.
[41]. S. Prbhakaran, Aniket Kulkarni, G. Vasanth, S. Kalainathan, Pratik Shukla, Vijay K. Vasudevan, Laser shock peening without coating induced residual stress distribution, wettability characteristics and enhanced pitting corrosion resistance of austenitic stainless steel [J], Applied

Surface Science, 428(2018) 17-30.
[42]. Vinodh Krishna Caralapatti, Sivakumar Narayanswamy, Analyzing the effect of high repetition laser shock peening on dynamic corrosion rate of magnesium [J], Optics and Laser Technology, 93(2017) 165-174.
[43]. Gene Whyman, Edward Bormashenko, Tamir Stein, The rigorous derivation of Yound, Cassie-Baxter and Wenzel equations and the analysis of the contact angle hysteresis phenomenon [J], Chemical Physics Letters, 450(2008) 355-359.
[44]. Anna Rudawska, Izabela Danczak, Miroslav Muller, Petr Valasek, The effect of sandblasting on surface properties for adhesion [J], International Journal of Adhesion&Adhesives, 70(2016) 176-190.
[45]. Seung Mi Baek, Myeong Hwan Shin, Jongun Moon, Ho Sang Jung, See Am Lee, WoonBong Hwang, Jong Taek Yeom, Sei Kwang Hahn and Hyoung Seop Kim, Superior pre-osteoblast cell response of etched ultrafine-grained titanium with a controlled crystallographic orientation [J], Scientific Reports, 7, 44213(2017).
[46]. Weihong Jin, GuosongWu, Hongqing Feng, Wenhao Wang, Xuming Zhang, Paul K. Chu. Improvement of corrosion resistance and biocompatibility of rare-earth WE43 magnesium alloy by neodymium self-ion implantation [J], Corrosion Science, 94(2015) 142-155.